





## Article

# System Simulation and Analysis of an LNG-Fueled SOFC System Using Additively Manufactured High Temperature Heat Exchangers

Jan Hollmann <sup>1,\*</sup>, Marco Fuchs <sup>1</sup>, Carsten Spieker <sup>2</sup>, Ulrich Gardemann <sup>2</sup>, Michael Steffen <sup>2</sup> and Xing Luo <sup>1</sup>  
and Stephan Kabelac <sup>1</sup>

<sup>1</sup> Institute of Thermodynamics, Leibniz University Hannover, 30167 Hannover, Germany; fuchs@ift.uni-hannover.de (M.F.); luo@ift.uni-hannover.de (X.L.); kabelac@ift.uni-hannover.de (S.K.)

<sup>2</sup> Zentrum für Brennstoffzellen Technik GmbH, 47057 Duisburg, Germany; c.spieker@zbt.de (C.S.); u.gardemann@zbt.de (U.G.); m.steffen@zbt.de (M.S.)

\* Correspondence: hollmann@ift.uni-hannover.de; Tel.: +49-511-762-4601

**Abstract:** A laboratory-scale solid oxide fuel cell (SOFC) system using liquefied natural gas (LNG) as a fuel is designed to be used as an energy converter on seagoing vessels (MultiSchIBZ project). The presented system design phase is supported by thermodynamic system simulation. As heat integration plays a crucial role with regard to fuel recirculation and endothermic pre-reforming, the heat exchanger and pre-reforming component models need to exhibit a high degree of accuracy throughout the entire operating range. Compact additively manufactured tube-bundle and plate-fin heat exchangers are designed to achieve high heat exchange efficiencies at low pressure losses. Their heat transfer correlations are derived from experimental component tests under operating conditions. A simulation study utilizing these heat exchanger characteristics is carried out for four configuration variants of pre-reforming and heat integration. Their system behaviour is analyzed with regard to the degree of pre-reforming and the outlet temperature of the fuel processing module. The combination of allothermal pre-reforming with additively manufactured plate-fin heat exchangers exhibits the best heat integration performance at nominal full load and yields a partial load capability to up to 60% electrical load at net electrical efficiencies of 58 to 60% (LHV).

**Keywords:** solid oxide fuel cell; fuel cell system design; maritime application; steam reforming; anode off-gas recirculation; additively manufactured heat exchangers



**Citation:** Hollmann, J.; Fuchs, M.; Spieker, C.; Gardemann, U.; Steffen, M.; Luo, X.; Kabelac, S. System Simulation and Analysis of an LNG-Fueled SOFC System Using Additively Manufactured High Temperature Heat Exchangers. *Energies* **2022**, *15*, 941. <https://doi.org/10.3390/en15030941>

Academic Editor: Orazio Barbera

Received: 18 December 2021

Accepted: 24 January 2022

Published: 27 January 2022

**Publisher's Note:** MDPI stays neutral with regard to jurisdictional claims in published maps and institutional affiliations.



**Copyright:** © 2022 by the authors. Licensee MDPI, Basel, Switzerland. This article is an open access article distributed under the terms and conditions of the Creative Commons Attribution (CC BY) license (<https://creativecommons.org/licenses/by/4.0/>).

## 1. Introduction

The decarbonization of the maritime sector is considered a major step to reduce the anthropogenic greenhouse gas (GHG) emissions responsible for global warming. According to the most recent International Maritime Organization (IMO) study, the global shipping sector caused up to 1.056 billion tons of CO<sub>2</sub> emissions in the year 2018, contributing to 2.89% of the global anthropogenic CO<sub>2</sub> emissions [1]. Heavy fuel oil and marine diesel oil remain up to now the dominant fuel types on seagoing vessels.

The IMO aims to reduce the maritime CO<sub>2</sub> emissions by half in 2050 compared to a 2008 reference level [2]. Besides technical and operational improvements (e.g., hydrodynamic ship designs, propulsion efficiency, voyage optimisation, etc.), the use of alternative fuels as well as the implementation of alternative energy converters are considered to be measures with the most significant impact [3]. The spectrum of fuel candidates ranges from lower-carbon fossil fuels like liquefied natural gas (LNG), methanol and biofuels to their synthetically produced counterparts from renewable energies like synthetic natural gas (SNG) to carbon free fuels like hydrogen and ammonia [4,5].

Apart from the main propulsion engine, auxiliary engines (AE), nowadays mostly heavy duty diesel generator sets are the second dominant GHG emitters on board, which

provide electrical energy for the vessel infrastructure (e.g., ship lighting, navigational instruments, manoeuvring thrusters, air conditioning, etc.). The average share of the AE on the overall fuel consumption highly depends on the vessel type and ranges from roughly 10% on seagoing container ships to up to 50% on cruise ships and refrigerated bulk carriers [1,6]. While the main engine is shut down during cargo time at ports, auxiliary engines are operated continuously unless electrical shorepower is available. This leads to continuous emissions of GHG as well as pollutants like nitrogen oxides (NO<sub>x</sub>), sulfur oxides (SO<sub>x</sub>) and particulate matter that pose a health risk, especially in ports close to residential areas [7].

The substitution of fossil fueled auxiliary combustion engines with more efficient energy converters like fuel cell systems is considered a major lever for reducing pollutants at sea and especially during cargo periods in ports. Compared to the conventional energy conversion pathway of diesel generator sets involving the intermediate steps of heat and mechanical power, fuel cells directly convert the internal chemical energy of a fuel into electrical energy. Above-mentioned by-products of combustion are almost avoided. Fuel cell systems for power generation are ideally implemented in a way that they run on the same fuel as the main propulsion engine and exhibit a broad fuel flexibility.

In the recent past until today, several research and prototype projects have been carried out that focus on the maritime application of fuel cells with present and potential future maritime fuels [8–10]. The majority of the recent projects regarding seagoing vessels focus on the application of high temperature polymer electrolyte membrane fuel cells (HT-PEMFC) [10,11] and solid oxide fuel cells (SOFC).

Commercial SOFCs typically use an oxygen ion conducting electrolyte that allows operation at temperatures of 500–850 °C. Due to the high temperatures, SOFC operation profits from fuel flexibility. It allows the direct supply of hydrocarbons like methane or methanol which are chemically converted to hydrogen at the anode catalyst surface via direct internal steam reforming (DIR). Additionally, SOFCs are capable of cracking ammonia into hydrogen and nitrogen [12].

Apart from several research projects using methanol [13] and ammonia [14] as a fuel, multiple SOFC research and application projects regarding LNG as a fuel have been reported, as an increasing number of modern seagoing vessels are equipped or planned with LNG fueled propulsion engines. Consequently, global LNG bunkering infrastructures at major ports have experienced a strong growth worldwide [15]. The EU project *NAUTILUS* has started in 2020 and enforces the installation of an LNG SOFC battery hybrid genset demonstrator designed for an implementation as an auxiliary power system on cruise ships [16]. A recent cooperation of Bloom Energy, Chantiers de l'Atlantique and MSC confirmed the installation of a 150 kW LNG-fueled SOFC pilot plant on board of the MSC World Europa [17]. Bloom Energy and Samsung Heavy Industries announced the equipping of a South Korean LNG carrier vessel with an SOFC system to substitute the propulsion and auxiliary engines [18].

The *SchIBZ* projects, funded by the German Federal Ministry of Transport and Digital Infrastructure (BMVI), have been working on the development of diesel and LNG based SOFC systems. Initially, research was focused on a diesel based SOFC demonstrator to prove the feasibility of a low-emission and efficient substitution of conventional auxiliary engines [19]. The demonstrator was realized as a container setup with a rated power of 50 kW<sub>el</sub>. Parallel to experimental system testing, a comprehensive thermodynamic system analysis was carried out to identify suitable operating conditions [20,21]. The experimental phase demonstrated the general proof of concept of the chosen system configuration. The follow-up project *MultiSchIBZ* has been concerned with process optimizations by means of novel high temperature heat exchanger concepts to increase the system compactness and power density. Additionally, scale-up measures to establish a container module with a rated power of 300 kW<sub>el</sub> as well as an additional pathway of LNG as a second fuel were investigated. The necessity of battery storage systems was analyzed to cope for the SOFC

ramp rates [22] and a techno-economic analysis was carried out to outline the economic efficiency of such SOFC systems in contrast to conventional auxiliary engines [23].

In the first *MultiSchIBZ* project phase, diesel and LNG laboratory systems were designed and built consisting of a modular SOFC module with a rated power of 15 kW<sub>el</sub> provided by the fuel cell manufacturer Sunfire GmbH and a fuel processing module, respectively. The design objective was focused on a scale-up concept that envisages a parallel setup of the modular fuel cell modules and a central fuel processing module being adapted in its size according to the targeted electrical output.

Experimental results of the prior project revealed modeling inaccuracies regarding the performance of the high temperature heat exchangers required for heat integration in the fuel recirculation and pre-reforming unit. In order to ensure the development of robust SOFC systems, a more detailed system model is required capable of adequately mapping heat integration over a wide range of operation. Compared to published models found in literature, the presented heat exchanger models exhibit a higher level of detail. A common assumption in published SOFC system modeling is the use of either a constant heat exchange effectiveness [24,25] or a constant overall heat transfer coefficient [26,27]. While this assumption may be true for the design operating point, the off-design characteristics occurring at flow conditions in partial load or other recirculation ratios cannot be mapped accurately, and the effectiveness is overestimated. The presented heat exchanger models exhibit heat transfer correlations that consider variations in mass flow and thermodynamical gas properties due to changes in gas composition comparable to work from Kupecki et al. [28,29]. The unique feature of this publication is the investigation of two different additively manufactured heat exchanger concepts (3D-HEX) and its impact on the overall system. The paper describes the entire development path from (1) the heat exchanger design optimization to (2) the experimental testing and deduction of suitable heat transfer correlations to (3) SOFC system modeling utilizing these component characteristics to investigate heat integration in full and partial load operation.

## 2. System Design

The development of fuel cell system designs has been focused on achieving high electrical system efficiencies. Regarding the use of methane as fuel for SOFCs, previous publications presented below already simulated different fuel processing system designs differing in their type of reforming (direct internal reforming (DIR), catalytic partial oxidation (CPOX) and steam pre-reforming (SR)). The latter variant can further be divided regarding the type of steam supply for the pre-reforming process by either recirculating condensed exhaust water or a share of the anode off-gas (AOG). Additionally, SR is either performed in an adiabatic or allothermal reactor by means of heat integration. The efficiencies in this paper refer to the net electrical output of the SOFC divided by the lower heating value (LHV) of the supplied fuel (see Equation (21)).

### 2.1. Overview of Investigated Methane-Fueled SOFC Systems

DIR concepts do not require an elaborate pre-reforming setup as all hydrocarbons react at the anode catalyst but are limited due to the high thermal gradients inside the fuel cell stack [30]. CPOX systems offer a low system complexity as well but yield a significantly smaller system efficiency compared to SR as experimentally shown by Mai et al. [31].

Regarding steam pre-reforming concepts, Peters et al. performed a comprehensive simulation parameter study for different water supply strategies including a water recirculation and AOG recirculation using a blower or an ejector [32]. The sub-variants differ in system complexity with respect to the number of components, the type of heat integration and the adiabatic or allothermal pre-reforming. The variants were investigated at nominal full electrical load with respect to the net LHV electrical efficiency as a function of the stack fuel utilization ( $FU_{\text{stack}}$ ) and the AOG recirculation ratio ( $RR$ , for definitions, see Equations (15) and (16)). Results show that the proposed system configurations with AOG recirculation by means of a blower generally achieve higher electrical efficiencies than the

variant with a closed water loop. High  $FU_{\text{stack}}$  and  $RR$  parameter settings are necessary to avoid carbon formation in the components, but should not be increased arbitrarily as the net system efficiency drops with increasing peripheral power demand of the blowers due to higher flow rates. Peters et al. determined a  $FU_{\text{stack}}$  of 60 to 80% at a  $RR$  of about 70% as the optimum operating range. The key parameters affecting the net efficiency are reported to be  $FU_{\text{stack}}$  and  $RR$ , followed by minor factors like the type of pre-reforming. A follow-up publication reports on an AOG recirculation system design with a recirculation temperature of 160 °C yielding net efficiencies of about 60% [33]. Both publications did not consider partial load behaviour and did not assume any heat losses.

Four different system configurations consisting of either allothermal or adiabatic SR and either water or AOG recirculation were investigated by van Biert et al. [34]. Results show that the systems with allothermal pre-reforming achieve higher electrical efficiencies and lower thermal gradients inside the stack than the adiabatic variants. Deviating from [32], the system with allothermal pre-reforming and water recirculation achieves slightly higher efficiencies than those with AOG recirculation. For a reliable system design, the authors consider it necessary to simulate both stack and system components in detail due to large interdependencies.

## 2.2. System Design Criteria

Apart from electrical system efficiency, the following criteria were chosen during the concept design phase of the laboratory system:

- **product safety** is influenced by the number of critical components which should be reduced to a minimum. Critical components are, for example, heat exchangers with a fuel gas and air or an oxygen-carrying medium, which can pose a safety risk on a ship and result in increased safety requirements.
- **development risk and availability of components** is minimized by selecting only commercially available components. In particular, this limits the AOG recirculation design as hydrogen compatible high-temperature blowers for temperatures above 300 °C are not available. Ejectors are available in principle or can be designed for the particular application but require a high pressure primary fluid (e.g., water or fuel) that ideally has a much higher density than the medium to be recirculated. Another disadvantage is the lack of modulation, which can cause problems especially at partial load operation.
- **robust heat integration** defines the amount of heat provided to temperature sensitive components like the pre-reformer. This influences the degree of pre-reforming and the system partial load capability. Optimal heat integration is done in a way that hot fluids with larger heat capacity rates supply heat to cold fluids with smaller heat capacity rates.
- **complexity of control** can be minimized by selecting a system design that can be operated stably via largely independent control loops.

## 2.3. Selected System Design

Figure 1 shows the proposed system configuration consisting of the Fuel Processing Module (FPM) and the Fuel Cell Module (FCM). The latter is a 15 kW<sub>e1</sub> module from Sunfire GmbH with 24 stacks of 30 3YSZ electrolyte supported cells each with an LSCF cathode and a Ni/GDC anode. The anode and cathode gas flows are supplied in parallel-flow configuration and are preheated to sufficient stack entry temperatures by counter-flow heat exchangers.

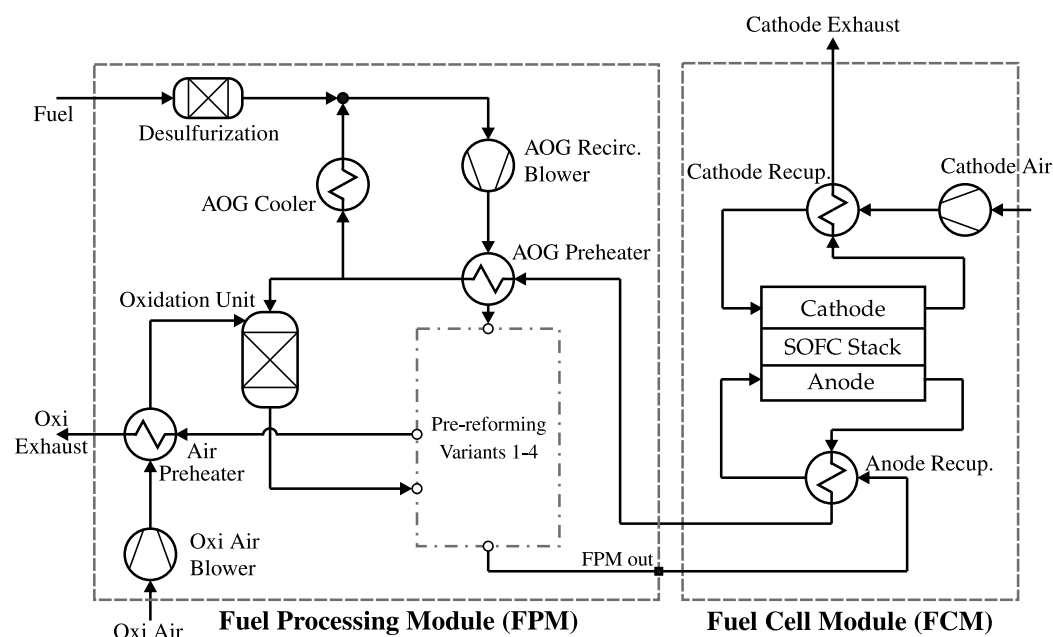


**Figure 1.** System configuration of the laboratory system including the fuel cell module (right) and fuel processing module (left) with a placeholder for the studied pre-reforming concept variants.

Following the results from the literature review in Section 2.1, the FPM is designed as a steam pre-reforming layout in combination with AOG recirculation at intermediate temperatures in order to achieve high efficiencies and to avoid the complexity of a closed water loop. In the selected variant, AOG enters the FPM with a temperature of about 600 °C and is cooled in the AOG Preheater. Part of the colder AOG is then passed through the AOG Cooler and mixed with the desulfurized fuel gas. The outlet temperature in the AOG Cooler is adjusted by means of cooling water or air so that the downstream mixture temperature matches the desired recirculation temperature. The AOG recirculation blower then conveys the mixture through the AOG Preheater, where it is heated up again for the following pre-reforming process. The remaining part of the AOG is fed to a catalytic burner (oxidation unit) where burnable components react with preheated air. The burner exhaust gas is used to first provide heat for pre-reforming and then to heat the combustion air in the Air Preheater.

Compared to system designs found in the above-mentioned publications, the FCM and FPM are only coupled in terms of the anode recirculation, whereas the cathode off-gas is not supplied to the oxidation unit. This is due to the fact that the required cathode volume flow to cool the stacks is much larger than the required air flow in the oxidation unit to yield the desired high outlet temperatures necessary for pre-reforming. Especially for a scaled-up configuration with multiple fuel cell modules, a direct cathode off-gas coupling would furthermore lead to larger volumes of the pipes and components downstream of the oxidation unit unnecessarily increasing installation space. Instead, the cathode off-gas flows may be used for cogeneration of useful heat for thermal processes on the vessel by means of additional heat exchangers outside the depicted system boundaries in Figure 1. For the laboratory system scale, these measures are not further investigated and are not part of this study.

#### 2.4. Pre-Reforming and Heat Integration Variants

As literature does not conclude to one optimal system design, different pre-reforming and heat integration concepts were investigated. Pre-reforming in Figure 1 is depicted by a placeholder that represents the four proposed pre-reforming variants shown in Figure 2.

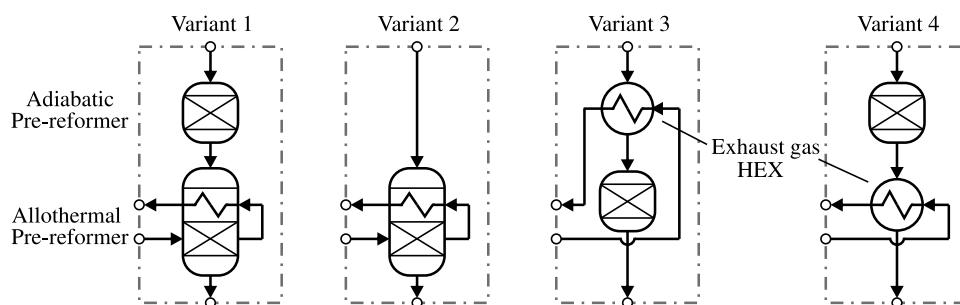


**Figure 2.** The four proposed pre-reforming variants.

The variants differ with regard to the sequence of heat integration and chemical reactions:

- Variant 1: a combination of adiabatic and allothermal pre-reforming, in which the heat for allothermal pre-reforming is provided by the oxidation unit exhaust gas.
- Variant 2: an allothermal pre-reforming in which the heat is provided by the oxidation unit exhaust gas.
- Variant 3: an upstream oxidation unit exhaust gas heat exchanger, followed by adiabatic pre-reforming.
- Variant 4: an adiabatic pre-reforming with a subsequent oxidation unit exhaust gas heat exchanger.

Each of the variants offers at least one specific advantage. A combination of two pre-reformers as in variant 1 is unusual, but results in an initial temperature drop in the adiabatic stage so that more heat can be transferred in the allothermal stage allowing a higher degree of pre-reforming. This is at the expense of higher and thus more cost-intensive use of catalyst material, higher pressure losses, and assembly space. Variant 2 thus has the advantage of less catalyst material, but at the cost of lower heat transfer in the allothermal pre-reformer and presumably lower outlet temperatures and degrees of pre-reforming. The least amount of catalyst material is used in the adiabatic variants 3 and 4, where the comparatively large allothermal pre-reformer can be replaced by smaller exhaust gas heat exchangers that do not require any catalyst bed. Variant 4 offers the advantage to modulate the FPM outlet temperature over a wider range via the burner temperature than in the other variants. However, this is at the expense of comparatively higher methane concentrations in the product gas. In variant 3, on the other hand, the degree of pre-reforming at the reformer outlet can be further reduced by the upstream exhaust gas heat exchanger compared with variant 4, but the FPM outlet temperature cannot be modulated as high as in variant 4. The impact of the four variants on the system performance will be discussed in Section 5.

Independent from the aforementioned pre-reforming variants, heat exchanger and reactor design were faced with the challenge of manufacturability and a low pressure loss demand in all stages, since the fuel cell stacks only allow pressure levels of 50 mbar (relative). As the installation on board of a vessel already leads to an exhaust gas back pressure of 10 to 15 mbar, this results in an average permissible maximum pressure loss of 5 mbar per FPM component. At the same time, high heat exchanger efficiencies have to be ensured to achieve high pre-reformer temperatures. Due to its flow gas compositions, the allothermal pre-reformer is considered as a critical component, which has to withstand high thermomechanical stress while maintaining gas tightness between the flows.

To meet the pressure loss criteria, the adiabatic pre-reformer is designed as a cylindrical reactor containing a precious-metal packed bed catalyst. The allothermal pre-reformer is designed as a conventional shell-and-tube heat exchanger with two bundles in cross-counter-flow configuration as depicted in Figure 3. The exhaust gas flows through the shell while the reformate gas first flows through one preheating tube bundle with empty tubes and subsequently through the reactor tube bundle containing a second packed bed catalyst. The use of a precious-metal catalyst is favored over Ni as it does not need to be reduced at the initial start-up. Furthermore, the disadvantage and safety risk of a typical Ni

catalyst regarding the pyrophoric behavior during an unanticipated exposition to oxygen is avoided. The oxidation unit is designed as a cylindrical reactor containing a monolithic honeycomb structured metal catalyst. Regarding the AOG Preheater and exhaust gas heat exchanger, compact and efficient heat exchangers with low pressure losses are required. Their design by means of additive manufacturing is presented in the following section.

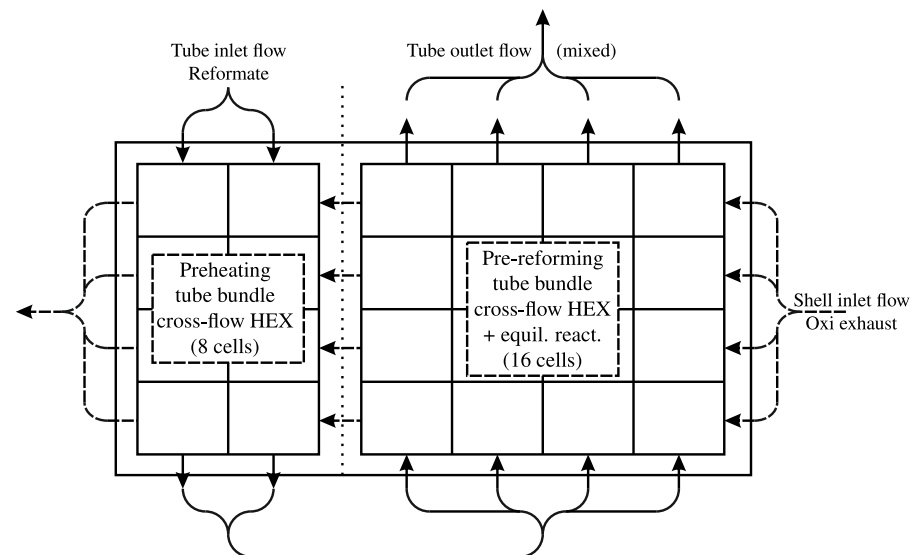


**Figure 3.** Visualization of the allothermal pre-reformer showing the flow distribution assumptions in the tube flow (solid lines) and shell flow (dotted lines).

### 3. Design and Characterization of Additively Manufactured High Temperature Heat Exchangers

Due to the limited installation space and increased safety requirements in the fuel processing module, the compact and non-gas leakage design of the heat exchangers is of decisive importance. Therefore, different types of heat exchangers are developed depending on the specific requirements. These include both tube bundle-based and plate-based heat exchangers. Due to the high degree of compactness and the increased safety requirements, these heat exchangers are manufactured using additive manufacturing, or more precisely, selective laser melting (SLM). Production using conventional methods, such as welding, might pose a safety concern as cross leakage might arise in the course of operating time and would not provide the required heat flux density of 0.5 kW/L. The heat exchangers developed are presented in detail below.

#### 3.1. Tube-Bundle Heat Exchanger (3D-TB-HEX)

The tube-bundle heat exchangers used in this project are designed in cross-counter-flow construction as illustrated in Figure 3. In this type of heat exchanger, the hot stream flows around the tube bundles and cools down, while the cold stream heats up accordingly inside the tubes. The number of deflections and thus the number of bundles determines the effectiveness of the heat exchanger. An increasing number of bundles can approximate the ideal counter-flow and the effectiveness increases. Depending on the design, this will happen at the expense of the pressure loss due to a longer “tube section”.

In order to meet the required power density, pressure loss and safety requirements, optimisations were made to the basic circular tube shape and measures are taken to increase heat transfer on the outside as well as on the inside surface. Additive manufacturing allows geometries to be produced that would not be feasible using conventional methods.

The general tube geometry is designed in a droplet shape. This reduces the wake area behind the tube for the shell-flow, leading to reduced pressure loss and increased heat transfer due to thinner thermal boundary layers. Additionally, the outside heat transfer area is increased with small fins. The geometry of the droplet shape is developed on the

basis of the numerical simulated flow (Ansys Fluent) around a circular tube bundle of five tubes and adapted according to the wake area behind the tubes. At first, numerical simulations of the heat transfer and pressure drop of a circular tube bundle with five tube rows were carried out. These results were then compared with literature data. The heat transfer coefficient differs less than 15% and the pressure drop less than 12% from the literature data, which is in the range of uncertainty for the literature data regarding circular tube banks [35,36]. Next, the geometry of the tube was modified to reduce the wake area behind the tubes. During this process, the mesh quality and independence as well as the flow field of the numerical calculation were permanently checked to ensure a valid calculation. After finding the best fitting tube geometry, additional fins were applied to the outside surface, increasing the heat transfer area by 81% with a fin efficiency of 97%. The pressure drop was increased by only 28% due to higher velocities in the narrowest sections between two tubes compared to the circular tubes.

On the inside of the droplet tube, a twisted tape is implemented that promotes swirl generation and turbulence for an increased heat transfer rate. By means of additive manufacturing, the twisted-tape is also connected to the tube wall leading to an increased heat transfer area in contrast to common tube inserts with a large contact resistance between insert and tube wall. An important parameter for the heat transfer and pressure drop of the twisted tape is the number of twists per unit length. Therefore, numerical simulations and also several experiments were carried out, testing different twist ratios and their influence on the heat transfer and pressure drop, as no valid Nusselt and pressure-drop correlations exist for this design and temperature range. As for the outside optimisation, the numerical and the experimental results are in good agreement with literature data for the basic circular tube, thus ensuring correct experimental and numerical data for the twisted-tape version. From these tests, the version with 10 twists per meter exhibits the best trade-off between the heat transfer and pressure drop increase. The optimized droplet shape and the small fins on the outside as well as the inserted twisted tape are shown in Figure 4. For the so-called 3D-TB-HEX, two bundles are used in a cross-counter-flow arrangement.

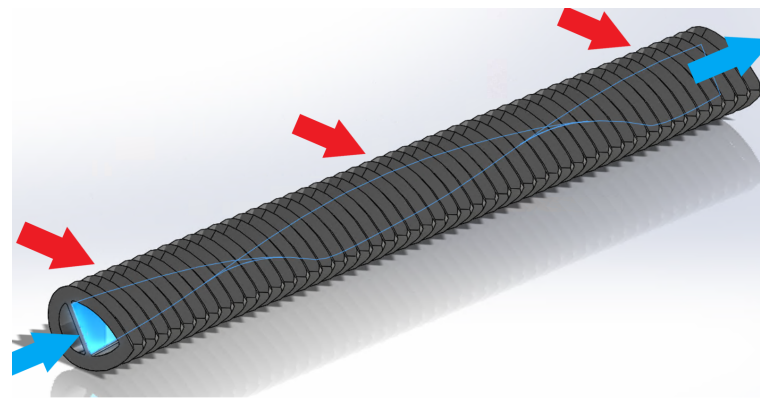


**Figure 4.** CAD model of a single tube of the 3D-TB-HEX. The helix structure of the internal twisted tape is depicted by means of blue contour lines.

### 3.2. Plate-Fin Heat Exchanger (3D-PF-HEX)

Another version of heat exchangers are plate-fin heat exchangers as they are characterised by a very high effectiveness due to the counter-flow characteristic [37]. “Wavy-fins” are chosen as the internal structure, as they are easy to manufacture due to their shape and contribute to the stability of the heat exchanger. The design of the heat exchanger, i.e., the determination of the structural parameters, was carried out using equations from literature and accompanied flow simulations with *OpenFoam* to extend the validity of the literature data. The results are also presented in Luo et al. [38]. In summary, the numerical simulation of the heat transfer agrees well with the experimental data from literature, while the numerical obtained pressure drop is lower as the experimental results in literature.



Based on the literature data, the geometric parameters of fin height, fin spacing, wavelength and amplitude are determined by optimisation with the constraints of maximum tolerable pressure loss and the most compact design possible. Further boundary conditions are the minimum wall thickness that can be printed and the maximum tolerable angle between a printed surface and the vertical printing axis. The global Matlab particle swarm algorithm is used for the optimisation. Due to the higher level of compactness of the plate-fin heat exchanger compared to the before presented tube-bundle heat exchanger, the effect of axial heat conduction in the solid parts (fins and plates) has been considered during the design process, as it has a significant negative impact on the overall performance. Figure 5 shows a section of the 3D-PF-HEX and the internal geometry. The construction volume of the plate-fin heat exchanger is approx. 1/4 of the 3D-TB-HEX at the same thermal load.

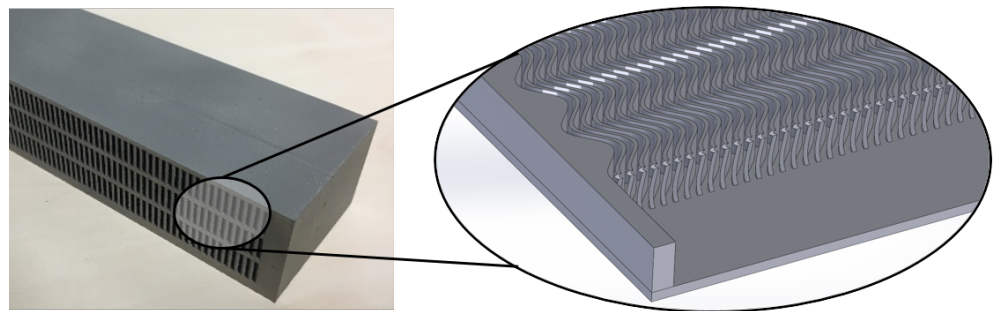


**Figure 5.** Close-up of the 3D-PF-HEX (left) and a CAD image of the internal fin geometry.

### 3.3. Experimental Validation

The heat exchangers presented above were manufactured from high-temperature stainless steel (1.4828) and tested experimentally in a separate test rig before being used in the fuel cell system in order to gain precise knowledge of the heat transfer performance as well as the pressure loss. The experimental setup is described in detail in [39]. Furthermore, the gas tightness at high temperatures is investigated by means of special tests. Based on the experimental data, equations for the pressure loss and the heat transfer are derived and then implemented in the later described system model in order to increase the model quality.

The 3D-TB-HEX and 3D-PF-HEX were each investigated at two different temperature levels. The inlet temperature of the hot side was varied between 560 °C and 750 °C by means of an electric heater, and the temperature of the cold side was varied between 200 °C and 250 °C. The mass flow was varied on both sides by two mass flow controllers between 0.2 and 0.7 kg/min, compressed air was used as the test fluid. The pressure loss was measured by two U-tube manometers.

In order to increase the accuracy of the air temperature measurement, all connections (fluid inlets and outlets) of the heat exchanger were additionally equipped with external heating to bring the temperature of the pipe wall closer to the measured gas temperature and thus reduce the influence of thermal radiation. These measures reduce the temperature difference between the respective pipe wall and the gas temperature measurement to less than 2K and significantly reduce negative thermal radiation influences.

To reduce heat losses, both heat exchangers were equipped with insulation made of a microporous insulating material. The insulation material also contained an opacifier to reduce losses due to thermal radiation, as the base material of the insulation becomes partially transparent at high temperatures. Figure 6 shows the insulated 3D-PF-HEX during installation.



**Figure 6.** Close-up of the insulated 3D-PF-HEX during installation at the described test rig.

### 3.4. Data Evaluation

From the temperatures obtained, the overall heat transfer coefficient  $UA_{\text{exp}}$  was obtained for each measuring point using the logarithmic temperature difference  $\Delta T_{\text{log}}$  and a correction factor  $F_{\text{Corr}}$  for counter-flow or cross-counter-flow characteristic (1):

$$UA_{\text{exp}} = \frac{\dot{Q}_c}{F_{\text{Corr}} \Delta T_{\text{log}}} = \left( \frac{1}{h_c A_c} + R_{\text{wall}} + \frac{1}{h_h A_h} \right)^{-1}, \quad (1)$$

with  $R_{\text{wall}}$  as the thermal wall conduction resistance and  $h_h$  and  $h_c$  as the heat transfer coefficients of the hot and cold fluid side, respectively. The correction factor  $F_{\text{Corr}}$  for the cross-counter-flow (and others) depends on the characteristic of the heat exchanger and is defined as the ratio of the effectiveness of any heat exchanger (in this paper the cross-counter-flow) compared to the ideal counter-flow heat exchanger:

$$F_{\text{Corr}} = \frac{\epsilon_{\text{CCF}}}{\epsilon_{\text{CF}}} \quad (F_{\text{Corr}} \leq 1). \quad (2)$$

Equation (1) cannot be solved directly for the unknown heat transfer coefficients  $h_c$  and  $h_h$ . Therefore, an optimisation algorithm is applied, using an error function given in Equation (3), containing the experimental overall heat transfer coefficient and a theoretical overall heat transfer coefficient of all measuring points (multi variable Wilson plot method):

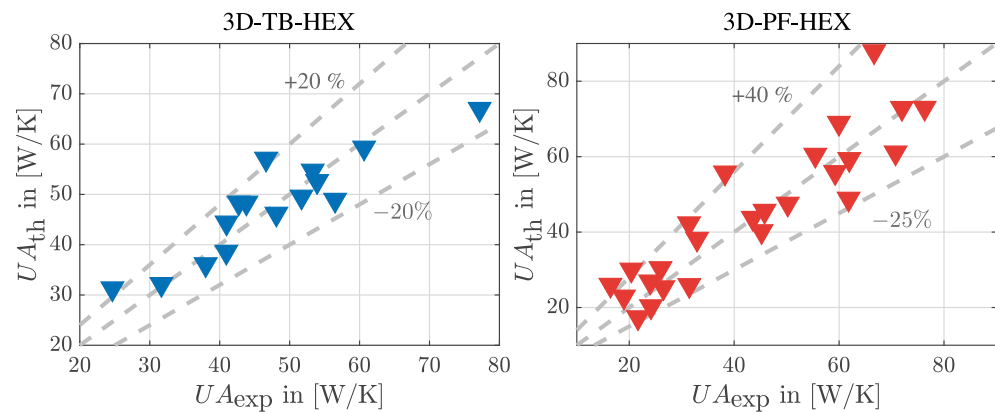
$$\min_{(\alpha_c, \alpha_h, \beta_c, \beta_h) \in \vec{x}} f(\vec{x}) = \sqrt{\frac{1}{N-1} \sum_{j=1}^N \left[ \frac{UA_{\text{th},j}(\vec{x})}{UA_{\text{exp},j}} - 1 \right]^2}. \quad (3)$$

The theoretical overall heat transfer coefficient  $UA_{\text{th},j}$  is calculated using the right side of Equation (1). For the two unknown heat transfer coefficients, typical basic Nusselt ( $Nu$ ) correlations for the heat transfer coefficients are used:

$$Nu_{c/h, \text{th},j} = \frac{h_{c/h, \text{th},j} \cdot d_{h, c/h}}{\lambda_{m, c/h,j}} = \alpha_{c/h} \cdot Re_{c/h,j}^{\beta_{c/h}} \cdot \sqrt[3]{Pr_{c/h,j}}, \quad (4)$$

with  $d_h$  as the hydraulic diameter,  $\lambda_m$  as the mean thermal conductivity,  $Re$  as the Reynolds number and  $Pr$  as the Prandtl number of the fluid flow. By varying the coefficients  $\alpha_c$ ,  $\alpha_h$ ,  $\beta_c$  and  $\beta_h$ , the Nusselt correlations for the heat transfer of both fluids are adjusted in such a way that the error value is minimised, i.e., the theoretical overall heat transfer coefficient matches the experimentally determined overall heat transfer as closely as possible. Figure 7

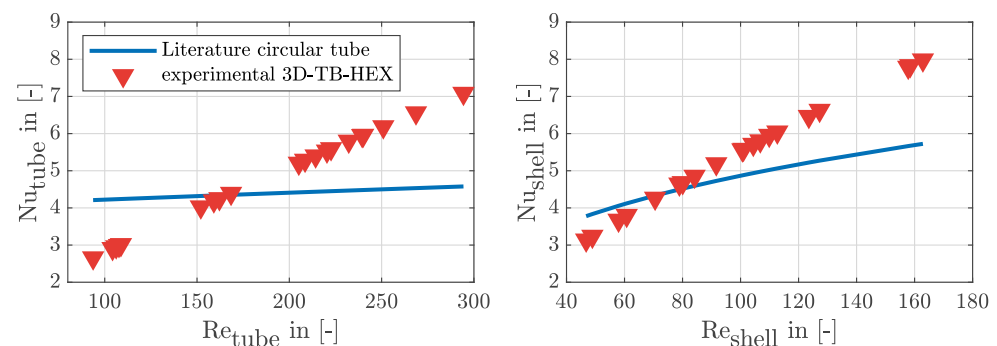
depicts the parity plots comparing the experimentally obtained and the deduced theoretical values of both heat exchangers along with reference lines and percentage deviations. As a result, equations for the heat transfer coefficient as a function of the Reynolds number are determined. The definitions for the Reynolds number, the hydraulic diameter as well as the Nusselt number for the tube-bundle and plate-fin heat exchanger can be found in the Appendices A.1 and A.2, respectively.



**Figure 7.** Comparison between the experimentally obtained overall heat transfer coefficient  $UA_{exp}$  and the theoretically calculated overall heat transfer coefficient  $UA_{th}$  using the parameterized Nusselt correlations (see Equation (4)) obtained from the experimental data.

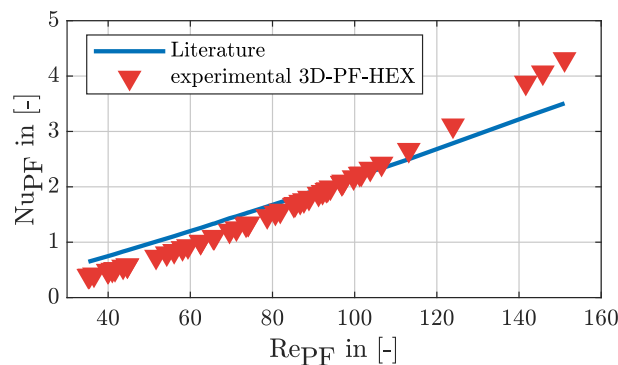
### 3.5. Experimental Results

Figure 8 shows the results of the determined Nusselt number for the tube and shell side of the 3D-TB-HEX as a function of the respective Reynolds number. From the data, it can be clearly seen that a lower Nusselt number is achieved with tube side Reynolds numbers below 160 and shell side Reynolds numbers below 75 compared to a conventional circular tube. The reason for this behaviour can be explained by the design of the heat exchanger. Due to the very low velocity, parasitic influences such as axial heat conduction within the tube wall as well as heat radiation gain influence, which have a negative effect on the performance and thus on the heat transfer coefficient. As a result of the integral evaluation procedure, this leads to a lowering of the Nusselt number. If the flow velocity is increased, the Nusselt number increases both on the tube side and on the shell side. At its peak, the Nusselt number is increased by 48% or 38%, compared to a smooth circular tube of the same hydraulic diameter.



**Figure 8.** Experimentally derived Nusselt numbers of the 3D-TB-HEX tube (left) and shell flow (right) as a function of the Reynolds number compared to the Nusselt numbers of a basic circular tube configuration calculated with correlations from literature [36]. The range of Reynolds numbers for the intended system application spans between 150 and 280 for the tube side and between 80 and 140 for the shell side.

Figure 9 shows the curve of the Nusselt number versus the Reynolds number for the 3D-PF-HEX. The blue solid line symbolises the Nusselt numbers determined from literature data [38] and the filled triangles represent the Nusselt numbers determined from the experiments. In contrast to the tube bundle, the literature data available here also correspond to those used for the design. Furthermore, the literature data presented here have already been extended to include the influence of axial heat conduction, but not the thermal radiation which also occurs, but on a significantly smaller scale. In the low Reynolds number range, the Nusselt numbers are lower than the corresponding literature data. With increasing Reynolds number, this behaviour changes and the Nusselt number exceeds the literature data starting at a Reynolds number of  $Re = 100$ .



**Figure 9.** Experimentally determined Nusselt numbers of the hot and cold 3D-PF-HEX flows as a function of the Reynolds number compared to the Nusselt numbers calculated with correlations from literature [38]. The range of Reynolds numbers for the intended system application spans between 80 and 130.

The reason for this slightly different behaviour between literature and measurement is due to an increasing measurement uncertainty in the low and high Reynolds number range. As a result of the low heat capacity currents, very high number of transfer units ( $NTU$ ; for the definition, see Equation (10)) and thus a very high effectiveness of over 98% is achieved. In combination with the asymptotic behaviour of the effectiveness as a function of the  $NTU$  value with a counter-flow apparatus [40], even small deviations or uncertainties in the temperature measurement lead to large changes in the  $NTU$  value and thus in the  $UA$  value and finally in the calculated heat transfer coefficient.

In the opposite case, i.e., with increasing Reynolds numbers ( $Re > 100$ ), the measurement uncertainty is also the main reason for the increasing deviation compared to the literature. The Nusselt numbers determined in this Reynolds number range were determined with unequal heat capacity ratios, the mass flow of the cold side, and thus its Reynolds number, was significantly smaller than that of the hot side. This also leads to a very high efficiency and thus also to an increasing measurement uncertainty of the  $UA$  value and finally to a higher uncertainty of the heat transfer coefficient, or the Nusselt number. In the medium Reynolds number range, the measurement results agree very well with the literature data, so that the underlying calculation model is well suited for predicting the effectiveness of the 3D-PF-HEX. The developed correlations of the Nusselt-Number for the 3D-TB-HEX as well as for the 3D-PF-HEX are used in the system modelling to increase its accuracy and to compare the impact of different kinds of heat exchanger on the overall system efficiency, see Section 5 for detailed comparison.

#### 4. Component Modelling and System Model

Component and system modelling was performed in *Matlab / Simulink* using the modelling infrastructure of the *Thermolib* toolbox version 5.3.2 from EUtech Scientific Engineering GmbH. Thermodynamic property data are provided by the NIST Webbook Database. The simulation setup is, in principle, dynamic in time, but, for this paper, it is used only to simulate steady-state operating points. Regarding the input streams of the

simulation model, the supplied LNG fuel is treated as pure methane. Depending on the fuel origin and treatment, LNG may also contain other components like higher hydrocarbons and nitrogen that may account for a share of up to 10 mol% [41] which are neglected in this study. It is assumed that a central LNG evaporation infrastructure is already present on the vessel so that the fuel enters the system fully evaporated at a supply pressure of 5 bar and ambient temperature (20 °C). In the maritime environment, the surrounding air is usually humid and contains NaCl which makes the system more susceptible to corrosion and catalyst poisoning. In this design, it is assumed that the cathode and oxidation blowers withdraw filtered and dehumidified air at ambient temperature from the surroundings of the system.

#### 4.1. Fuel Cell Stack

The fundamental stationary 0D-SOFC model has been presented in a previous publication [20], where it was used in a diesel-fueled SOFC simulation model and validated for stationary operating points. For this study, the model was adapted to the employed stack design regarding the number of cells, the area specific resistance (ASR) and expected heat losses.

The essential features of the model include internal methane steam reforming (MSR) and water gas shift (WGS) reactions (see Equations (11) and (12)) at the anode surface. The remaining methane is converted completely. For the WGS reaction, chemical equilibrium at the outlet temperature is assumed. The cell model comprises an energy balance by means of a thermal mass representing the interconnect and cell material. It is assumed that the anode and cathode outlet flows leave the stack at the thermal mass temperature  $T_{\text{stack}}$ . Deviating from the previous model description in [20], the electrochemical voltage losses are described in a simplified form using an exponentially temperature dependent area specific resistance (ASR) equation that represents the almost linear current voltage characteristic of electrolyte supported cells [33,42]:

$$ASR(T_{\text{stack}}) = ASR_0 \cdot \exp \left[ \frac{E_a}{R_m} \left( \frac{1}{T_{\text{stack}}} - \frac{1}{T_0} \right) \right], \quad (5)$$

with  $ASR_0$  as the reference ASR at reference temperature  $T_0$  in Kelvin,  $E_a$  as the activation energy and  $R_m$  as the molar gas constant. The ASR of the electrolyte supported cell at beginning of life is located around the value of 650 mΩ cm<sup>2</sup> at reference temperature of 850 °C [43]. Due to its 0D limitation, the model is not capable of calculating the local temperature, current density, ASR and gas composition distribution along the flow path inside the stack. The presented model was fitted to operation data provided by a 1D stationary model of the stack manufacturer comparable to *along the channel* models shown in [42,44] by adjusting the mean ASR value  $ASR_0(T_{\text{stack}})$ . Similar temperatures and gas compositions of the anode and cathode outlet flows as well as cell voltages could be mapped compared to the more detailed 1D model. Operating points were defined at given electric currents, inlet temperatures, gas compositions as well as fuel and oxygen utilization.

#### 4.2. Heat Exchangers

All heat exchangers except the anode and cathode recuperators as well as the AOG Cooler are modelled using the *NTU* method. The fluid with the smaller heat capacity rate  $\dot{C}_{\text{min}} = \min(\dot{C}_c; \dot{C}_h)$  determines the maximum possible heat transfer rate  $\dot{Q}_{\text{max}}$  [45]:

$$\dot{Q}_{\text{max}} = \dot{C}_{\text{min}} \cdot (T_{h,\text{in}} - T_{c,\text{in}}) \quad (6)$$

The performance of the heat exchanger can be expressed as its effectiveness  $\epsilon$  by relating the actual heat transfer rate  $\dot{Q}$  to the maximum heat transfer rate  $\dot{Q}_{\text{max}}$ :

$$\epsilon = \frac{\dot{Q}}{\dot{Q}_{\text{max}}} = \frac{\dot{C}_c(T_{c,\text{out}} - T_{c,\text{in}})}{\dot{C}_{\text{min}}(T_{h,\text{in}} - T_{c,\text{in}})} = \frac{\dot{C}_h(T_{h,\text{in}} - T_{h,\text{out}})}{\dot{C}_{\text{min}}(T_{h,\text{in}} - T_{c,\text{in}})} \quad (7)$$

The following effectiveness relations can be derived as shown in [45] for a counter-flow configuration:

$$\epsilon_{co} = \frac{1 - \exp(-NTU(1 - C_r))}{1 - C_r \cdot \exp(-NTU \cdot (1 - C_r))} \quad (8)$$

and a cross-flow configuration with both fluids unmixed:

$$\epsilon_{cr} = 1 - \exp\left(\frac{NTU^{0.22}}{C_r} \left(\exp(-C_r \cdot NTU^{0.78}) - 1\right)\right) \quad (9)$$

Apart from the flow configuration, the effectiveness is a function of the number of transfer units ( $NTU$ ) by setting the product of the overall heat transfer coefficient  $U$  and heat exchange area  $A$  in relation to the smaller heat capacity flow as well as the ratio between the smaller and larger heat capacity rate  $C_r$  given by the formulas:

$$NTU = \frac{UA}{\dot{C}_{min}} \quad \text{and} \quad C_r = \frac{\dot{C}_{min}}{\dot{C}_{max}} \quad (10)$$

Deviating from the previous publication [20], the overall heat transfer coefficients  $U$  required in Equation (10) are not held constant, but are calculated as a function of geometry, flow configuration, mass flow and thermal properties of the fluids. This allows the evaluation of the heat exchanger performance within the entire operating range. The product of the overall heat transfer coefficient  $U$  and the heat exchange area  $A$  is calculated using Equation (1) with the heat transfer coefficients  $h_{c/h}$  for the cold and hot side and the thermal resistance of the wall  $R_{wall}$ .

Different Nusselt correlations are used to calculate these heat transfer coefficients depending on the geometry and flow conditions. An overview of the correlations used for each component is provided in Table 1. The correlation equations are either specified in detail in Appendix A or taken from experimental results (Section 3).

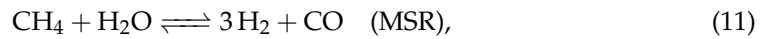
For the anode and cathode plate recuperators, the effectiveness is determined by an operating map deducted from datasets provided by the manufacturer using the mass flows and inlet temperatures of the component as input variables. As the AOG Cooler does not contribute to heat integration, AOG cooling is modelled as a change in enthalpy to the desired temperature.

**Table 1.** Overview of heat exchanger models and their Nusselt correlations.

Component Name	Model Description	Correlations
Anode and Cathode Recup.	Convent. counter-flow HEX	Operating map
Air Preheater	Convent. cross-counter-flow tube bundle HEX	Appendix A.1
Allothermal Pre-reformer	Convent. cross-counter-flow tube bundle HEX (2 bundles, 1 empty, 1 filled with catalyst) Cell model with 24 HEX and equilibrium reaction cells	Appendix A.1
AOG Preheater	3D cross-counter-flow tube bundle HEX or 3D counter-flow plate fin HEX	Experimental Equation (4)
Exhaust Gas Heat exchanger	3D cross-counter-flow tube bundle HEX or 3D counter-flow plate fin HEX	Experimental Equation (4)

#### 4.3. Pre-Reforming

Both inside the SOFC stack and the pre-reforming reactors, MSR and WGS reactions take place simultaneously:



In the pre-reformer stages, it is assumed that chemical conversion occurs until chemical equilibrium is reached. In reality, this assumption may not be reached at lower temperatures and leads to significant deviations between simulated and experimental gas compositions. With regard to the studied laboratory system, the assumption is kept as a precious metal catalyst with a high activity compared to typically used Ni catalysts is used. Additionally, the pre-reformers are designed big enough to ensure a high residence time. The gas mixture leaves the reactor at equilibrium reaction temperature and composition. Carbon formation reactions are not considered. In the Oxidation Unit, the remaining AOG burnable components are catalytically converted completely.

In the allothermal pre-reformer, heat exchange and chemical reactions occur simultaneously and inhomogeneously. Due to the cross-flow configuration and temperature dependent chemical equilibrium, temperature distribution and chemical conversion are expected to be distributed significantly between the tube rows. A discrete 2D cell model was chosen as presented by Engelbracht et al. [33] (see Figure 3). Homogeneous flow distribution and an unmixed shell flow are assumed. Each cell consists of a combination of an *NTU* heat exchanger and an additional equilibrium reactor on the cold fluid side. Based on a grid independence study ranging from six to up to 48 cells, a total of 24 cells was chosen to map the component behaviour at a reasonable computation time.

#### 4.4. Blowers and Pressure Losses

Component pressure losses are modelled as a function of the involved mass flow:

$$\Delta p_{\text{comp},i} = k_{\text{comp},i} \cdot \dot{m}_{\text{comp},i}^2 \quad (13)$$

As specific component pressure losses regarding the FPM heat exchangers, pre-reformers and the oxidation unit are not yet experimentally available, the maximum design value of 5 mbar specified during the component design phase is used for each FPM component in the simulation model (compare Section 2.4). The pressure loss coefficients  $k_{\text{comp},i}$  are determined by assuming these maximum permissible pressure losses at the component mass flows  $\dot{m}_{\text{comp},i}$  during nominal full load operation.

The peripheral electrical power demand is estimated by considering the cathode, recirculation and combustion air blowers depicted in Figure 1 assuming constant isentropic and mechanical efficiencies as done in [34].

#### 4.5. Heat Losses

All components and pipes of the laboratory-scale FPM are separately thermally insulated to ensure accessibility during testing. Heat transfer between the components and ambient are estimated by means of steady-state thermal analyses of the laboratory setup in ANSYS Mechanical using the geometrical design and insulation properties. Overall heat transfer coefficients are deducted and implemented into the component and pipe models to represent temperature dependent heat losses:

$$\dot{Q}_{\text{loss},i} = (U \cdot A)_{\text{amb},i} \cdot (T_{\text{comp},i} - T_{\text{amb}}) \quad (14)$$

#### 4.6. System Parameters and Operating Conditions

A set of widely common system parameters is used to define and confine the system operating range. The required excess of fuel and oxygen flow provided at the respective electrodes is characterized by the electrochemical stack fuel and oxygen utilizations:

$$FU_{\text{stack}} = \frac{\dot{n}_{\text{An,in}}(x_{\text{H}_2,\text{in}} + x_{\text{CO},\text{in}} + 4x_{\text{CH}_4,\text{in}}) - \dot{n}_{\text{An,out}}(x_{\text{H}_2,\text{out}} + x_{\text{CO},\text{out}})}{\dot{n}_{\text{An,in}}(x_{\text{H}_2,\text{in}} + x_{\text{CO},\text{in}} + 4x_{\text{CH}_4,\text{in}})} \cdot 100\%, \quad (15)$$

$$OU_{\text{stack}} = \frac{0.21\dot{n}_{\text{Ca,in}} - \dot{n}_{\text{Ca,out}}x_{\text{O}_2,\text{out}}}{0.21\dot{n}_{\text{Ca,in}}} \cdot 100\%. \quad (16)$$

The amount of AOG recirculated is defined by the recirculation ratio:

$$RR = \frac{\dot{n}_{\text{AOG,rec}}}{\dot{n}_{\text{AOG,total}}} \cdot 100\% \quad (17)$$

Both  $RR$  and  $FU_{\text{stack}}$  impact the overall system fuel utilization:

$$FU_{\text{sys}} = \frac{FU_{\text{stack}}}{1 - RR(1 - FU_{\text{stack}})} \quad (18)$$

as well as the gas composition of the pre-reforming inlet flow as the recirculated AOG is mixed with the fuel flow. The oxygen to carbon ratio  $O/C$  is a parameter typically used in literature to depict the pre-reforming gas composition by means of element balancing:

$$O/C = \frac{2x_{\text{CO}_2,\text{pre}} + x_{\text{CO},\text{pre}} + x_{\text{H}_2\text{O},\text{pre}}}{x_{\text{CO}_2,\text{pre}} + x_{\text{CO},\text{pre}} + x_{\text{CH}_4,\text{pre}}} = f(RR, FU) \quad (19)$$

The effect of carbon formation has not been modeled in this study and depends on the ternary  $H/O/C$  gas composition and temperature [34,46]. The  $O/C$  value itself does not describe this relation sufficiently. However,  $O/C$  values given in the following section serve as comparative values to the above-mentioned publication results.

Analogous to Equation (16), the oxygen utilization of the oxidation unit  $OU_{\text{oxi}}$  defines the excess oxygen in relation to a complete stoichiometric combustion and is defined as the ratio of non-recirculated molar flows of combustible AOG components to the provided oxygen molar flow:

$$OU_{\text{oxi}} = \frac{(1 - RR) \cdot \dot{n}_{\text{AOG,total}} \cdot (0.5x_{\text{H}_2,\text{AOG}} + 0.5x_{\text{CO},\text{AOG}})}{0.21\dot{n}_{\text{oxi,air}}} \cdot 100\% \quad (20)$$

It is assumed that the SOFC system feeds into an AC electric board infrastructure requiring a frequency inverter which exhibits a conversion efficiency of  $\eta_{\text{pe}} = 95\%$  [34]. Overall system performance is evaluated using the net system energetic efficiency:

$$\eta_{\text{sys,net}} = \frac{|P_{\text{el,SOFC,DC}}| \cdot \eta_{\text{pe}} - (P_{\text{el,bl,ca}} + P_{\text{el,bl,rec}} + P_{\text{el,bl,oxi}})}{\dot{n}_{\text{fuel,in}} \cdot LHV_{\text{fuel,in}}} \quad (21)$$

To specifically investigate the pre-reforming variants in terms of their capability to convert high amounts of methane into hydrogen, the so-called degree of pre-reforming ( $DOR_{\text{pre}}$ ) is defined as used in [47]:

$$DOR_{\text{pre}} = \frac{\dot{n}_{\text{fuel,in}} - \dot{n}_{\text{CH}_4,\text{FPM,out}}}{\dot{n}_{\text{fuel,in}}} \cdot 100\% \quad (22)$$

relating the amount of converted methane in all pre-reformer stages via endothermic MSR to the supplied fuel flow. The  $DOR_{\text{pre}}$  mainly correlates with the achievable pre-reforming outlet temperature. The remaining percentage is converted at the SOFC anode inlet via DIR.

The definition of an operating point is specified by the following system input parameters:



- the electrical current  $I$ .
- the stack fuel utilization  $FU_{\text{stack}}$  and the recirculation ratio  $RR$  which determine the molar flow of the supplied fuel  $\dot{n}_{\text{fuel,in}}$ .
- the stack oxygen utilization  $OU_{\text{stack}}$  which defines the cathode molar flow and is manipulated to control the stack outlet temperature  $T_{\text{stack}}$  to a set point of 815 °C.  $OU_{\text{stack}}$  is limited upwards to a value of 35% to ensure a sufficient oxygen partial pressure at the cathode.
- the oxygen utilization of the oxidation unit  $OU_{\text{oxi}}$  which defines the supplied air flow in the FPM and is manipulated to control the oxidation unit outlet temperature  $T_{\text{oxi,out}}$  to a set point of 750 °C.  $OU_{\text{oxi}}$  is limited upwards to a value of 80% to ensure a complete combustion of the non-recirculated combustible components.
- the heat flow withdrawn from the anode off-gas in the AOG Cooler which is manipulated to control the recirculation blower inlet temperature  $T_{\text{bl,rec,in}}$  to a set point of 300 °C. In case of recirculation temperatures below this value, the AOG Cooler is inactive and does only contribute in terms of its heat losses.

Depending on the electrical current, the stack temperature as well as the anode and cathode inlet properties, the SOFC model determines the resulting cell voltage which acts as output variable along with the electrical DC power  $P_{\text{el,SOFC,DC}}$  and the net system efficiency  $\eta_{\text{sys,net}}$ . The SOFC inlet temperatures are variable and depend on the performance of the anode and cathode heat exchangers as well as the FPM outlet stream conditions. The stack operation is restricted by the minimum stack temperature and the minimum cell voltage which are given in Table 2 as part of a complete list of system parameter constraints.

**Table 2.** Constraints and selected operating range of the system parameters. Bold printed values depict the nominal full load operating point.

System Parameters		Unit	Constraints	Input Values/ Set Points
Electrical current	$I$	[A]		20, <b>30</b>
Recirculation ratio	$RR$	[%]		56... <b>70</b> ...80
Oxygen to carbon ratio	$O/C$	[-]	$\geq 2.0$	2.0... <b>2.55</b> ...3.0
Stack fuel utilization	$FU_{\text{stack}}$	[%]	$\leq 75$	<b>75</b>
Stack oxygen utilization	$OU_{\text{stack}}$	[%]	$\leq 35$	*
Oxid. unit oxygen utilization	$OU_{\text{oxi}}$	[%]	$\leq 80$	*
Cell voltage	$U_{\text{cell}}$	[V]	$\geq 0.65$	**
Recirc. blower inlet temperature	$T_{\text{bl,rec,in}}$	[°C]	$\leq 300$	300
Stack outlet temperature	$T_{\text{stack}}$	[°C]	750...850	815
Oxidation unit outlet temperature	$T_{\text{oxi,out}}$	[°C]	$\leq 750$	750
Isentropic blower efficiency	$\eta_{\text{bl,is}}$	[%]		70
Mechanical blower efficiency	$\eta_{\text{bl,mech}}$	[%]		80
Power electronics efficiency	$\eta_{\text{pe}}$	[%]		95

\*: manipulated within the allowed range to control the respective temperature to its set point. \*\*: output variable.

#### 4.7. Parameter Study

To analyze the steady-state operating behavior, a parameter study is conducted covering an operating range depicted in the right column of Table 2. The system is operated at the maximum  $FU_{\text{stack}} = 75\%$ . Higher utilizations, especially at high recirculation ratios, pose the risk of Ni reoxidation at the anode surface [48], whereas lower utilizations would lead to a decrease in the electrical efficiency and lower stack temperatures due to endothermic DIR. The recirculation ratio is set over a range of 56 to 80%. This corresponds to a system fuel utilization of 87.2 to 93.8% and an O/C ratio of 2.0 to 3.0 at the chosen maximum  $FU_{\text{stack}}$  operation. Full and partial load performance is considered by lowering the electric current from the nominal operating point of 30 A to 20 A. A maximum recirculation temperature set point of 300 °C is selected for the highest possible heat integration.

Each of the pre-reforming variants presented in Section 2.4 is simulated in two configurations which differ in the heat exchanger models used for the AOG Preheater and the exhaust gas heat exchanger (if implemented). The first configuration employs the cross-counter-flow 3D-TB-HEX described in Section 3.1 and the second configuration the more efficient and compact counter-flow 3D-PF-HEX described in Section 3.2. The properties of the system inlet and outlet streams for variant 1 using the 3D-PF-HEX at nominal full load operation as defined in Table 2 are presented in the Appendix A.3.

## 5. Simulation Results and Discussion

The overall stationary system behaviour is presented for full and partial load operation followed by the analysis of an additional partial load operating strategy. As not all system parameters mentioned above can be displayed, system performance is discussed by means of the  $DOR_{pre}$  (see Equation (22)), the system net efficiency  $\eta_{sys,net}$  (see Equation (21)) as well as temperature levels of the AOG recirculation, the pre-reforming outlet and the stack.

### 5.1. Full Load Operating Points

At all simulated full load operating points, the stack outlet temperature set point is reached as the exothermic electrochemical reaction dominates the SOFC energy balance, and excess air is needed to cool the stacks. The recirculation ratio defines not only the  $O/C$  ratio of the pre-reforming gas mixture, but also the heat capacity rates ( $\dot{C} = \dot{n} \cdot C_{p,m}$ ) of both fluids involved in the heat transfer taking place in the allothermal pre-reformer or exhaust gas heat exchanger. At  $RR$  below 65%, the mean heat capacity rate of the hot oxidation unit exhaust gas is larger than the heat capacity rate of the pre-reforming gas ( $\dot{C}_h > \dot{C}_c$ ). In this case, the heat flow is defined by the heat capacity rate  $\dot{C}_c = \dot{C}_{min}$  according to Equation (6). At larger  $RR$ , this behaviour reverses as  $\dot{C}_c > \dot{C}_h = \dot{C}_{min}$ . This is caused by the increase of the molar flow of the recirculated stream  $\dot{n}_{AOG,rec}$  with simultaneous decrease of the exhaust gas flow as less fuel is supplied to the oxidation unit and less air is required to remain at the constant oxidation unit exhaust temperature. The mean molar heat capacities  $C_{p,m}$  of the fluids change as well due to changing recirculation gas compositions and different oxygen utilizations at the oxidation unit, but have a significantly smaller and counteracting impact on the heat capacity rates, therefore slightly dampening the impact of the molar flow change.

Figure 10a shows the resulting degree of pre-reforming  $DOR_{pre}$ , indicating the overall FPM heat integration performance. The four variant configurations using 3D-TB-HEX are displayed as solid lines, whereas the counterpart models with 3D-PF-HEX are depicted as dotted lines. Variant 1 with the 3D-TB-HEX shows a high methane conversion in the range of  $RR < 65\%$  with  $DOR_{pre}$  values of 32%. This is due to favorable heat capacity ratios both in the AOG Preheater and the allothermal pre-reformer as mentioned above. No heat has to be withdrawn in the recirculation unit as the recirculation temperature remains below 300 °C (see Figure 10b). As the  $RR$  increases above 68%, this temperature limit is reached due to worse heat capacity ratios in the AOG Preheater. The higher the recirculation ratio, the more heat has to be withdrawn in the AOG Cooler resulting in lower  $DOR_{pre}$  levels of 28%.

Comparing this behaviour to the configuration with 3D-PF-HEX, one can clearly see the positive impact of the higher effectiveness of the AOG Preheater. At low  $RR$ , the pre-reforming inlet temperature increases by 35 K leading to higher  $DOR_{pre}$  of up to 34%. The more significant difference occurs at higher  $RR$ . The  $DOR_{pre}$  remains at a constant level of 33% as the AOG recirculation temperature reaches its limit not before an  $RR$  of 76% leading to a higher level of heat integration (see Figure 10b). Regarding the nominal full load operating point at  $RR = 70\%$ , the configuration with a 3D-PF-HEX AOG Preheater does not require AOG cooling in the recirculation unit.

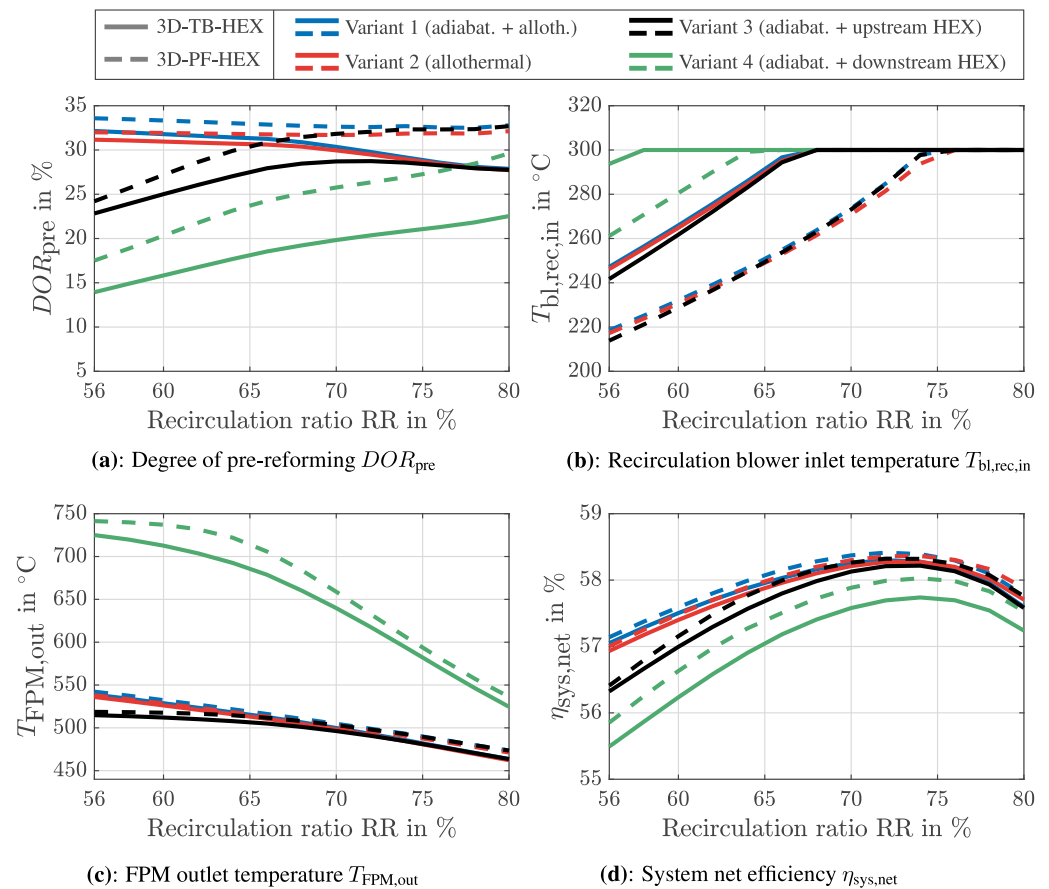


**Figure 10.** Simulation results for full load operating points ( $I = 30$  A) at maximum stack fuel utilization  $FU_{stack} = 75\%$  as a function of the AOG recirculation ratio  $RR$ .

In general, both heat exchanger configurations of variant 2 show a similar behavior compared to their variant 1 counterparts. Due to the missing adiabatic pre-reforming stage and its favorable temperature drop regarding heat transfer in the following allothermal pre-reformer, both configurations of variant 2 yield lower  $DOR_{pre}$  values of 0.5 to 1%-points. The purely adiabatic variants 3 with an upstream exhaust gas heat exchanger behave similarly at high recirculation ratios but lose performance at lower  $RR$ . This is due to the fact that less heat can be transferred in the upstream exhaust gas heat exchanger compared to the allothermal heat transfer with a simultaneous endothermic reaction.

As variant 4 features an adiabatic pre-reformer with downstream superheating, the FPM outlet temperatures, displayed in Figure 10c, are located in a much higher range than the previous variants (470 to 550 °C) leading to higher anode inlet temperatures. This is caused by the fact that the required heat of reaction in the adiabatic pre-reformer needs to be supplied indirectly via the anode gas loop and thus heavily depends on heat losses and the effectiveness of the AOG Preheater. As the exhaust gas heat exchanger also lifts the AOG temperature, the AOG recirculation temperature already reaches its limit at much lower recirculation ratios (see Figure 10b), leading to high levels of heat being withdrawn from the system. As a consequence, the  $DOR_{pre}$  values of variant 4 with 3D-TB-HEX are significantly lower leading to higher levels of DIR. Out of the four variants, variant 4 features the highest sensitivity towards heat exchanger effectiveness. With both AOG Preheater and exhaust gas heat exchanger designed as 3D-PF-HEX, the  $DOR_{pre}$  increases by up to 7%-points but is almost entirely below the levels of the other variants.

The system net efficiencies depicted in Figure 10d generally increase with higher  $RR$  due to an increase in the system fuel utilization  $FU_{sys}$  but are limited by the electric demand of the recirculation blower leading to the decrease at  $RR > 75\%$ . Comparing the course of

the variants, deviations of up to 0.5%-points at the nominal operating point of  $RR = 70\%$  are visible.

### 5.2. Partial Load Operating Points

As the electrical current is decreased, the dissipated heat from electrochemical conversion in the stack decreases accordingly, whereas heat losses remain almost the same. Excess air cannot be decreased arbitrarily due to the  $OU_{stack}$  constraint leading to decreasing stack temperatures. For all simulated operating points at 20 A (corresponding to 62 to 68% of electrical net power at full load), the OU limitation already leads to higher cathode air flows than thermally required. Besides artificially heating the cathode inlet flow by means of electric heating, supplying the stack with anode gas at a high temperature and high degree of pre-reforming remains the only option in order to maintain permissible stack temperatures.

Figure 11a shows the  $DOR_{pre}$  of the four variants. In general, the depicted values are substantially smaller than for the presented full load operating points, opposing the intended partial load behaviour mentioned above. One main effect is that the heat losses do not decrease proportionately to the component mass flows resulting in higher temperature drops inside the components and pipes. A second impact is the decline of heat transfer coefficients due to smaller mass flows. Variants 1 and 2 no longer remain in ranges above 30% but decrease towards 20% for high RR. Unlike full load operation, both configurations of variant 3 slightly exceed the  $DOR_{pre}$  levels of variants 1 and 2. This indicates that heat transfer at partial load in the additively manufactured exhaust gas heat exchangers is more effective than in the allothermal pre-reformer with conventional tube bundles. Variant 4 again yields the lowest  $DOR_{pre}$  levels with high FPM outlet temperatures at the same time (see Figure 11c).

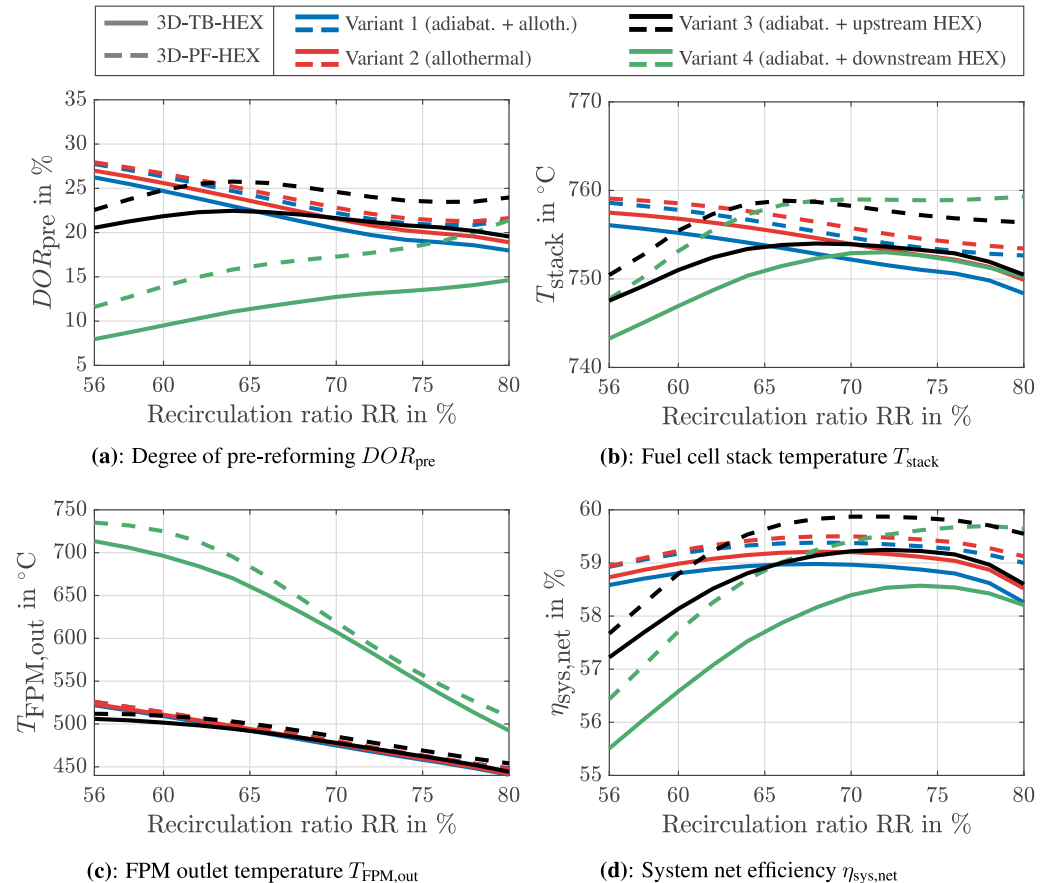


**Figure 11.** Simulation results for partial load operating points ( $I = 20$  A) at maximum stack fuel utilization  $FU_{stack} = 75\%$  as a function of the AOG recirculation ratio  $RR$ .

The resulting stack temperatures are depicted in Figure 11b. All variants show temperatures close to the minimum permissible limit of 750 °C with the adiabatic 3D-PF-HEX variants 3 and 4 yielding slightly higher temperatures at RR around 70%. The partial load efficiencies shown in Figure 11d are generally higher than the full load efficiencies as the cell voltage increases due to lower voltage losses. However, the depicted lower stack temperatures lead to higher ASR values partly counteracting this effect. The highest efficiency of nearly 60% is achieved by variant 3 using 3D-PF-HEX.

As a further load decrease towards 50% of the nominal electrical load would violate the stack temperature constraint, a heat integration countermeasure is investigated to increase the system operating range.

### 5.3. Measures for Increasing FPM Performance at Partial Load

In order to further increase the partial load capability of the FPM at lower electrical currents, higher degrees of pre-reforming are required. This is realised by increasing the hot mass flow in the allothermal pre-reformer or exhaust gas heat exchanger by means of additional supply of fuel to the oxidation unit being catalytically converted which is already part of the startup heating process. The oxidation unit is further controlled to a set point of 750 °C. Hereafter, only the 3D-PF-HEX variants are considered due to their better impact on FPM heat integration. The amount of additional fuel supplied to the oxidation unit compared to the conventional operation in the previous section is given by the oxidation unit surplus fuel ratio  $SFR_{oxi}$ :

$$\dot{n}_{fuel,oxi} = SFR_{oxi} \cdot \dot{n}_{fuel,in} \quad (23)$$

relating the molar flow of fuel added to the oxidation unit to the molar flow supplied to the AOG recirculation. The system efficiency has to be adapted regarding the increased fuel input:

$$\eta_{sys,net,SFR} = \frac{|P_{el,SOFC,DC}| \cdot \eta_{pe} - (P_{el,bl,ca} + P_{el,bl,rec} + P_{el,bl,oxi})}{\dot{n}_{fuel,in}(1 + SFR_{oxi}) \cdot LHV_{fuel,in}} \quad (24)$$

Simulations were conducted for the four 3D-PF-HEX variants at 20A partial load, maximum  $FU_{stack}$  and a recirculation ratio of 70%. The  $SFR_{oxi}$  was varied between 0% (equivalent to operating points depicted in Figure 11 at RR = 70%) and 20%.

Figure 12a depicts the degree of pre-reforming as a function of the surplus fuel in the oxidation unit. An increase of FPM performance is visible for all four variants and stack temperatures rise accordingly (see Figure 12b). Up to an  $SFR_{oxi}$  of 5%, variants 1, 2 and 3 behave similarly by increasing to  $DOR_{pre}$  values of 33% which is equivalent to the levels achieved in full load operation (see Figure 10a). The behaviour changes as variant 3 converges to a maximum of 39% due to the heat transfer limitation in the exhaust gas heat exchanger. The allothermal variants continue to rise to levels above 50%. Variant 4 remains at rather low pre-reforming levels of 25%.

As displayed in Figure 12b, allothermal pre-reforming of variants 1 and 2 are able to lift the stack temperature to its set point leaving the  $OU_{stack}$  control limitation. The adiabatic variants only lead to a maximum increase of 22 K. Regarding the system efficiency, a surplus fuel ratio of 5% decreases the partial load efficiency by 1.5%, whereas a surplus fuel ratio of 15% leads to a decrease of 5% for allothermal variants. The adiabatic configurations decrease further to up to 6.5%-points as the ASR of the SOFC is higher due to lower stack temperatures.

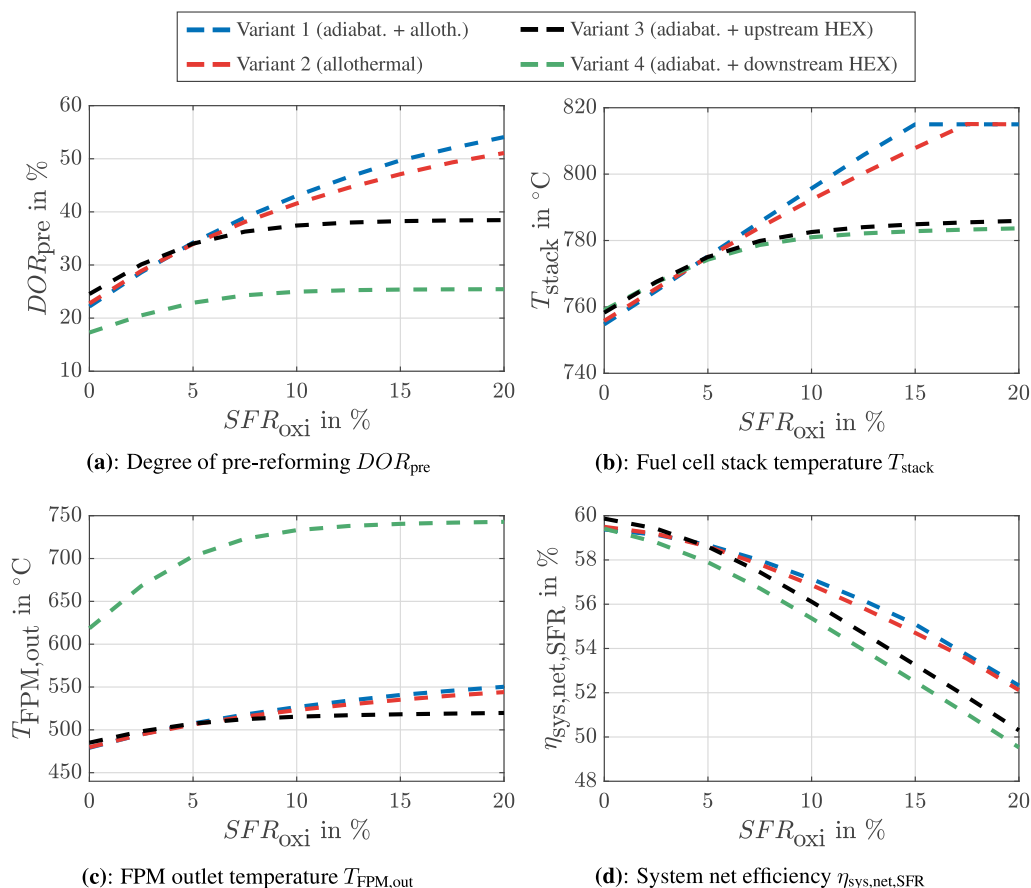


**Figure 12.** Simulation results for partial load operating points with additional fuel supplied to the oxidation unit ( $I = 20$  A) at maximum stack fuel utilization  $FU_{stack} = 75\%$  as a function of the surplus fuel ratio  $SFR_{oxi}$ .

#### 5.4. Discussion

In accordance with literature, allothermal AOG recirculation variants exhibit the best pre-reforming results regarding full load operation. Operating points with a high fuel utilization and a recirculation ratio of 70% yield the highest full load system efficiencies. A more sophisticated heat integration by means of more efficient heat transfer in the AOG Preheater enables higher degrees of pre-reforming, especially at higher recirculation ratios. All investigated variants are in principle suited for the depicted full load operating range. In terms of heat integration, variant 4 with a downstream exhaust gas heat exchanger is less suitable for the presented FPM configuration as more heat has to be withdrawn in the recirculation loop. Its pre-reforming performance is highly sensitive to heat losses and heat transfer effectiveness.

Regarding the risk of carbon formation in the pre-reformer stages, the operating range might be limited at lower  $RR$ . According to more profound equilibrium models found in literature, carbon formation is thermodynamically favourable at  $O/C$  values below 2.5 ( $RR$  of 66% at maximum  $FU_{stack}$ ) at a temperature of 500 °C [32,34], which roughly corresponds to the simulated pre-reformer outlet temperatures at nominal full load operation (compare Figure 10c). However, this simplified comparison is limited, as (a) the equilibrium temperatures increase for lower  $RR$  to values up to 545 °C and (b) precious-metal catalysts exhibit a higher barrier towards carbon formation compared to Ni catalysts [49]. Eventually, the actual operating range limitation needs to be experimentally validated which will be reported in a future publication.

Regarding the system design criteria described in Section 2.2, the variants 1, 2 and 3 in combination with 3D-PF-HEX offer the advantage of a higher product safety and a less complex control. The AOG Cooler as a potentially critical component (if cooled

with air) is not required for a large part of the full load operating range ( $RR \leq 76\%$ , see Figure 10b) and can therefore be removed. The recirculation temperature does not have to be controlled actively but may be monitored instead. If recirculation temperature reaches high levels, the recirculation ratio may be adapted to slightly lower values by means of the recirculation blower.

In this simulation study, partial load behaviour and its limitation due to thermal restrictions become more apparent than in other publications. This is due to the detailed simulation level of the comparatively high heat losses caused by the laboratory setup as well as the decreasing heat transfer coefficients at lower mass flows. As depicted in Figure 11, partial load is limited to roughly 60% of electrical net power at full load due to low stack temperature levels that can be slightly lifted by means of the more efficient 3D-PF-HEX. Both adiabatic variants show a slight advantage due to a higher heat transfer effectiveness compared to the conventionally built allothermal pre-reformer. A further temperature increase at all studied variants can be realized by means of additional fuel supply in the oxidation unit. As shown in Figure 12b, the allothermal variants 1 and 2 allow a generally higher amount of heat integration, which enables these variants to further decrease the electrical load at the price of decreasing system efficiencies. The thermal robustness and partial load capability are expected to increase substantially when the system is scaled up as described in Section 1.

The system model accuracy will be investigated in detail in a follow-up publication by means of experimental data of stationary full and partial load operating points. Based on the presented simulation results, the laboratory-scale system was planned, designed and built according to variant 1 due to the most efficient full load behavior and the ability to supply the highest amount of heat via additional fuel in the oxidation unit at partial load. Component integration was realized in such a way that a change to the other pre-reforming variants remains possible for further investigation by either removing or replacing the adiabatic or allothermal pre-reformer with an additional heat exchanger. The AOG Cooler is implemented into the recirculation loop so that the entire operating range remains accessible. The component may be removed if experimental results confirm the system behaviour.

Further process improvements regarding heat integration could be performed in future by applying the successful compact additive manufacturing designs to the allothermal pre-reformer. This would merge the higher heat transfer rates of allothermal pre-reforming with a higher heat transfer effectiveness enabling even lower partial load operation without supplying additional fuel to the oxidation unit. In addition, a more detailed 1D-stack model as shown in [44] would provide a more profound knowledge regarding thermal gradients inside the stack along the flow channel.

## 6. Conclusions

Within the framework of the *MultiSchIBZ* project, an LNG-fueled SOFC laboratory-scale system was simulated, designed and built to investigate the full and partial load behaviour. The objective of the presented work was to choose an efficient and thermally robust fuel processing configuration suitable for a given fuel cell module with a rated electrical power of 15 kW<sub>e1</sub>. The fuel processing module (FPM) was designed considering a scale-up concept for future applications supplying multiple fuel cell modules in parallel in a containerized setup on board of seagoing vessels.

Based on a wide range of fuel processing concepts shown in literature, an anode off gas recirculation concept with methane steam pre-reforming was selected to achieve high system efficiencies. A recirculation temperature of 300 °C was chosen based on the availability of commercial recirculation blowers.

Hydrocarbon-fueled SOFC systems with intermediate temperature anode recirculation and pre-reforming require a high level of heat integration to ensure sufficient pre-reforming temperatures and thus operability without the risk of carbon formation. To ensure this, a system simulation model in *Matlab/Simulink* was equipped with heat exchanger and

pre-reformer models exhibiting heat transfer correlation functions to adequately map the mass flow and gas composition dependencies. High temperature heat exchangers were specifically designed and built for the desired application by means of additive manufacturing using selective laser melting. Two types of heat exchangers, a tube bundle cross-counter-flow (3D-TB-HEX) and a plate fin counter-flow (3D-PF-HEX) configuration, were experimentally tested in a separate test rig at flow conditions similar to the intended application in the FPM. Individual Nusselt correlations were deduced allowing reliable mapping of heat transfer.

Utilizing the obtained heat exchanger characteristics, a system simulation study was performed investigating heat integration of four system designs by means of the degree of pre-reforming, each with a setup of the 3D-TB-HEX or 3D-PF-HEX being used in the anode recirculation. As a key component regarding heat integration, the allothermal pre-reformer was designed as a 2D discretized model assuming chemical equilibrium in each cell, therefore not considering kinetics of the reforming and water-gas shift reaction.

Results show that allothermal variants deliver the highest degree of pre-reforming throughout the investigated range of anode recirculation ratios at nominal electric load. Using the counter-flow 3D-PF-HEX, heat exchange effectiveness and thus the level of overall heat integration is increased both in full and partial load compared to the 3D-TB-HEX. Highest net electrical efficiencies of 58 to 60% are obtained at maximum fuel stack utilization and an anode recirculation ratio of 70%. A suitable strategy to further increase the partial load capability has been presented by supplying a surplus fuel share of up to 5% to the catalytical afterburner which increases the FPM and stack outlet temperatures significantly at the cost of slightly lower net efficiencies.

In summary, system simulation has proven the applicability of the presented system configuration. As a consequence, the allothermal variant with an additional adiabatic upstream stage (called variant 1 in this study) was chosen to be built as a laboratory system for proof of concept and to support the scale-up design by means of model validation. The system was installed at the laboratory of Zentrum für BrennstoffzellenTechnik GmbH and equipped with an appropriate number of temperature and pressure sensors as well as a gas analysis infrastructure. The experimental results will be published in a follow-up publication.

**Author Contributions:** Conceptualization, J.H., M.F., C.S. and X.L.; methodology, J.H., M.F., C.S. and X.L.; software, J.H. and C.S.; formal analysis, J.H., M.F. and C.S.; investigation, J.H., M.F. and C.S.; writing—original draft preparation, J.H., M.F. and C.S.; visualization, J.H. and M.F.; writing—review and editing, supervision, project administration and funding acquisition, U.G., M.S. and S.K. All authors have read and agreed to the published version of the manuscript.

**Funding:** The authors gratefully acknowledge the financial support by the Federal Ministry of Transport and Digital Infrastructure, Germany (BMVI, funding code 03B10605H) and the coordination of the *MultiSchIBZ* project by the National Organisation Hydrogen and Fuel Cell Technology (NOW GmbH), Germany.

**Acknowledgments:** The authors gratefully thank Wolfgang Bender from Hülsenbusch Apparatebau GmbH & Co. KG and Philipp Schwarz from Rosswag GmbH for providing the two heat exchangers for experimental testing.

**Conflicts of Interest:** The authors declare no conflict of interest.

## Abbreviations

The following abbreviations are used in this manuscript:

3D-HEX	additively manufactured heat exchanger
AE	auxiliary engine
AOG	anode off-gas
CPOX	catalytic partial oxidation



DIR	direct internal reforming
FCM	fuel cell module
FPM	fuel processing module
GHG	greenhouse gas
HEX	heat exchanger
IMO	International Maritime Organization
LHV	lower heating value
LNG	liquefied natural gas
MSR	methane steam reforming
MultiSchIBZ	Multiple SchiffsIntegration Brennstoffzellen (German: ship integration of multiple fuel cell (modules))
PF	plate fin
SchIBZ	SchiffsIntegration Brennstoffzellen (German: ship integration of fuel cell (modules))
SLM	selective laser melting
SNG	synthetic natural gas
SOFC	solid oxide fuel cell
TB	tube bundle
WGS	water gas shift

## Nomenclature

### Roman symbols

$A$	area [m <sup>2</sup> ]
$ASR$	area specific resistance [ $\Omega\text{cm}^2$ ]
$\dot{C}$	heat capacity rate [W K <sup>-1</sup> ]
$C_r$	ratio of heat capacity rates [-]
$d_h$	hydraulic diameter [m]
$DOR_{pre}$	degree of pre-reforming [%]
$E_a$	activation energy [J mol <sup>-1</sup> ]
$F_{corr}$	correction factor for cross-counter-flow [-]
$FU_{stack}$	stack fuel utilization [%]
$h$	heat transfer coefficient [W m <sup>-2</sup> K <sup>-1</sup> ]
$I$	electrical current [A]
$k$	coefficient for component pressure loss [Pa s <sup>2</sup> kg <sup>-2</sup> ]
$\dot{m}$	mass flow [kg s <sup>-1</sup> ]
$\dot{n}$	molar flow [mol]
$NTU$	number of transfer units [-]
$Nu$	Nusselt number [-] s <sup>-1</sup>
$O/C$	oxygen to carbon ratio [-]
$OU$	oxygen utilization [%]
$p$	pressure [Pa]
$P_{el}$	electrical power [W]
$Pr$	Prandtl number [-]
$\dot{Q}$	heat transfer rate [W]
$Re$	Reynolds number [-]
$R_m$	molar gas constant [J mol <sup>-1</sup> K <sup>-1</sup> ]
$RR$	AOG recirculation ratio [%]
$R_{wall}$	thermal resistance of HEX wall [K W <sup>-1</sup> ]
$SFR_{oxi}$	Surplus fuel ratio (oxidation unit) [%]
$T$	temperature [°C]
$u$	velocity [m s <sup>-1</sup> ]
$U$	overall heat transfer coefficient [W m <sup>-2</sup> K <sup>-1</sup> ]
$x$	molar fraction [-]

### Greek symbols

$\alpha$	proportional Nusselt coefficient [-]
$\beta$	exponential Nusselt coefficient [-]
$\epsilon$	heat exchanger effectiveness [-]
$\eta$	efficiency [%]
$\lambda$	thermal conductivity [W m <sup>-1</sup> K <sup>-1</sup> ]
$\nu$	kinematic viscosity [m <sup>2</sup> s <sup>-1</sup> ]
$\psi$	void fraction [-]

### Subscripts

0	reference
amb	ambient
bl	blower
co	counter-flow
comp	component
cr	cross-flow
el	electrical
exp	experimental
fuel	fuel inlet flow
is	isentropic
lam	laminar
mech	mechanical
oxi	oxidation unit
pe	power electronics
pf	plate fin
pre	pre-reforming
rec	recirculation
sys	system
tb	tube bundle
th	theoretical
turb	turbulent

## Appendix A. Reynolds- and Nusselt-Number Definitions

### Appendix A.1. Definitions for Tube Bundle Heat Exchangers and Reformers

According to [36], the Reynolds number of the tube flow is defined as:

$$Re_{\text{tube}} = \frac{u_{\text{tube}} d_{h,\text{tube}}}{\nu_{\text{tube}} \psi_{\text{HR}}}, \quad (\text{A1})$$

with the flow velocity  $u_{\text{tube}}$ , tube-side hydraulic diameter  $d_{h,\text{tube}} = d_i$ , kinematic viscosity  $\nu_{\text{tube}}$  and void fraction  $\psi_{\text{HR}} = 1$  for empty tubes and  $\psi_{\text{HR}} = 0.4$  for tubes filled with catalyst bulk (ideal sphere packing).

The shell flow Reynolds-Number is defined analogously [36]:

$$Re_{\text{shell}} = \frac{u_{\text{shell}} d_{h,\text{shell}}}{\nu_{\text{shell}} \psi_{\text{shell}}}, \quad (\text{A2})$$

with the hydraulic diameter  $d_{h,\text{shell}} = \frac{\pi}{2} d_a$  and the void fraction  $\psi_{\text{shell}}$  for the shell side:

$$\psi_{\text{shell}} = 1 - \frac{\pi}{4a}, \quad (\text{A3})$$

with the lateral pitch ratio  $a$  of the tube bundle geometry.

On the tube flow side, the Nusselt number  $Nu_{\text{tube}}$  is deduced from the combined correlations of the two heat transfer boundary conditions (constant wall temperature and constant heat flux) to determine the heat transfer coefficient  $h_{\text{tube}}$  [36]:

$$Nu_{\text{tube}} = \frac{h_{\text{tube}} \cdot d_{h,\text{tube}}}{\lambda_{\text{tube}}} = 4.01 + 0.00319 \cdot Re_{\text{tube}}^{0.911}. \quad (\text{A4})$$

On the shell flow side, the Nusselt correlation for staggered tube-bundles is used [36]:

$$Nu_{\text{shell}} = \frac{h_{\text{shell}} \cdot d_{h,\text{shell}}}{\lambda_{\text{shell}}} = \left( 0.3 + \sqrt{Nu_{\text{lam}}^2 + Nu_{\text{turb}}^2} \right) \cdot f_A, \quad (\text{A5})$$

$$Nu_{\text{lam}} = 0.664 \cdot \sqrt{Re_{\text{shell}}} \sqrt[3]{Pr_{\text{shell}}}, \quad (\text{A6})$$

$$Nu_{\text{turb}} = \frac{0.037 Re_{\text{shell}}^{0.8} Pr_{\text{shell}}}{1 + 2.443 Re_{\text{shell}}^{-0.1} \left( Pr_{\text{shell}}^{2/3} - 1 \right)}, \quad (\text{A7})$$

$$f_A = 1 + \frac{0.7}{\psi_{\text{shell}}^{1.5}} \frac{b/a - 0.3}{(b/a + 0.7)^2}, \quad (\text{A8})$$

with the longitudinal pitch ratio  $b$  and the Prandtl number  $Pr_{\text{shell}}$ .

The coefficients to describe the Nusselt correlation for the 3D-TB-HEX used in Equation (4) are determined as follows:  $\alpha_{c,TB} = 0.402$ ;  $\beta_{c,TB} = 0.86$ ;  $\alpha_{h,TB} = 0.234$ ;  $\beta_{h,TB} = 0.75$ .

### Appendix A.2. Definitions for Plate-Fin Heat Exchangers

The definition of the Reynolds-Number for the plate-fin type heat exchanger is similar to the tube bundle heat exchangers but is typically defined using the mass velocity (or mass flux)  $\dot{G}_{\text{PF}} = \dot{m}_{\text{PF}} / A_c$ , with  $A_c$  as the free flow area in the finned part:

$$Re_{\text{PF}} = \frac{\dot{G}_{\text{PF}} d_{h,\text{PF}}}{\eta_{\text{PF}}}, \quad (\text{A9})$$

with the hydraulic diameter  $d_{h,\text{PF}} = \frac{2s_f h_f}{s_f + h_f}$  with  $s_f$  as fin spacing and  $h_f$  as fin height.

The coefficients to describe the Nusselt correlation for the 3D-PF-HEX used in Equation (4) are determined as follows:  $\alpha_{c,\text{PF}} = \alpha_{h,\text{PF}} = 0.00126$ ;  $\beta_{c,\text{PF}} = \beta_{h,\text{PF}} = 1.64$ .

## Appendix A.3. Stream Data at Nominal Full Load Operating Point

Stream properties		Cathode Air	Cathode Exh.	Fuel	Oxi Air	Oxi Exhaust
$\dot{n}$	mol/s	1.166	1.109	0.0308	0.113	0.200
$T$	°C	20.0	175.5	20.0	20.0	253.4
$p$	bar	1.013	1.036	5.0	1.013	1.028
$x_{O_2}$	mol%	21	17	0	21	9
$x_{N_2}$	mol%	79	83	0	79	45
$x_{CH_4}$	mol%	0	0	100	0	0
$x_{H_2O}$	mol%	0	0	0	0	31
$x_{CO_2}$	mol%	0	0	0	0	15

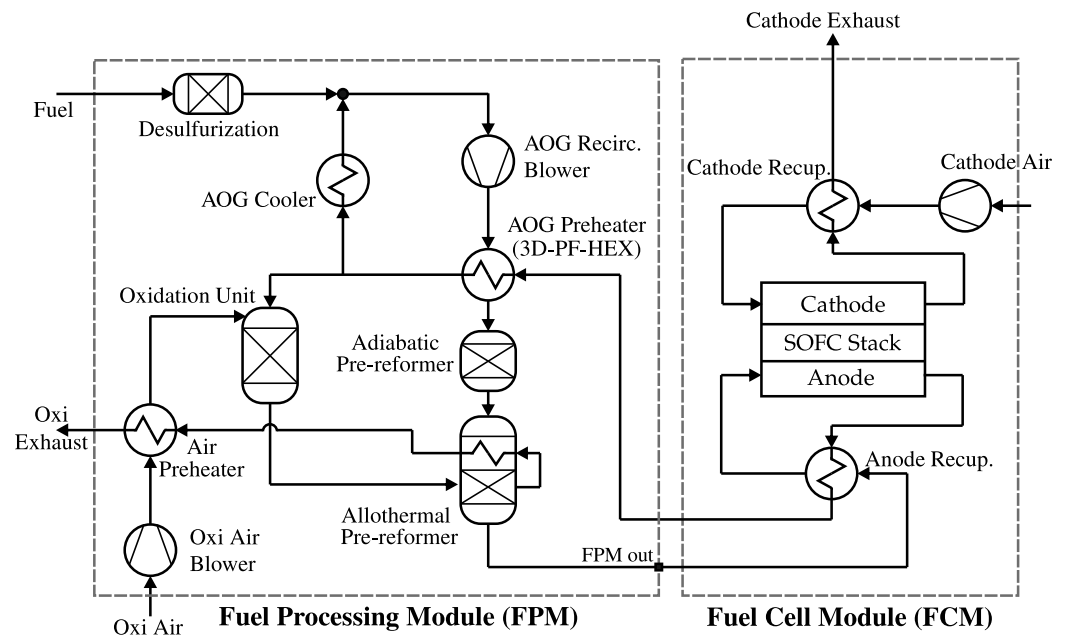


**Figure A1.** Properties of the system inlet and outlet streams at nominal full load operating point for variant 1 using the counter-flow 3D-PF-HEX.

## References

- International Maritime Organization. *Fourth Greenhouse Gas Study 2020*; International Maritime Organization: London, UK, 2020.
- International Maritime Organization. *Adoption of the Initial IMO Strategy on Reduction of GHG Emissions from Ships and Existing IMO Activity Related to Reducing GHG Emissions in the Shipping Sector*; International Maritime Organization: London, UK, 2018.
- Xing, H.; Spence, S.; Chen, H. A comprehensive review on countermeasures for CO<sub>2</sub> emissions from ships. *Renew. Sustain. Energy Rev.* **2020**, *134*, 110222. [CrossRef]
- DNV GL AS Maritime. *Comparison of Alternative Marine Fuels*. 2019. Available online: [https://sea-Ing.org/wp-content/uploads/2020/04/Alternative-Marine-Fuels-Study\\_final\\_report\\_25.09.19.pdf](https://sea-Ing.org/wp-content/uploads/2020/04/Alternative-Marine-Fuels-Study_final_report_25.09.19.pdf) (accessed on 18 December 2021).
- Bicer, Y.; Dincer, I. Clean fuel options with hydrogen for sea transportation: A life cycle approach. *Int. J. Hydrogen Energy* **2018**, *43*, 1179–1193. [CrossRef]
- European Commission. *2020 Annual Report on CO<sub>2</sub> Emissions from Maritime Transport: Report from the Commission*; European Commission: Brussels, Belgium, 2021. Available online: [https://ec.europa.eu/clima/document/download/3eb00f74-c7ba-4dd1-8ea6-18f6f135053e\\_en](https://ec.europa.eu/clima/document/download/3eb00f74-c7ba-4dd1-8ea6-18f6f135053e_en) (accessed on 18 December 2021).
- Chu-Van, T.; Ristovski, Z.; Pourkhesalian, A.M.; Rainey, T.; Garaniya, V.; Abbassi, R.; Jahangiri, S.; Enshaei, H.; Kam, U.S.; Kimball, R.; et al. On-board measurements of particle and gaseous emissions from a large cargo vessel at different operating conditions. *Environ. Pollut. (Barking Essex 1987)* **2018**, *237*, 832–841. [CrossRef] [PubMed]
- van Biert, L.; Godjevac, M.; Visser, K.; Aravind, P.V. A review of fuel cell systems for maritime applications. *J. Power Sources* **2016**, *327*, 345–364. [CrossRef]
- Xing, H.; Stuart, C.; Spence, S.; Chen, H. *Fuel Cell Power Systems for Maritime Applications: Progress and Perspectives*. *Sustainability* **2021**, *13*, 1213. [CrossRef]
- Leites, K. Fuel Cells for Marine Applications. In *Fuel Cells*; Stolten, P.D., Samsun, D.R.C., Garland, D.N., Stolten, D., Garland, N., Samsun, R.C., Eds.; Wiley-VCH: Weinheim, Germany, 2016; pp. 202–207. [CrossRef]
- Bloom SOFC to power Korean LNG ship. *Fuel Cells Bull.* **2021**, *2021*, 8. [CrossRef]
- Rathore, S.S.; Biswas, S.; Fini, D.; Kulkarni, A.P.; Giddey, S. Direct ammonia solid-oxide fuel cells: A review of progress and prospects. *Int. J. Hydrogen Energy* **2021**, *46*, 35365–35384. [CrossRef]

13. Barrett, S. (Ed.) METHAPU prototypes methanol SOFC for ships. *Fuel Cells Bull.* **2008**, *5*, 4–5. [CrossRef]
14. Barrett, S. (Ed.) ShipFC project on first maritime fuel cell to run on green ammonia. *Fuel Cells Bull.* **2020**, *2*, 5–6. [CrossRef]
15. SEA-LNG. LNG as a Marine Fuel—Our Zero Emissions Future Starts Now, 2020. Available online: [https://sea-lng.org/wp-content/uploads/2020/02/200214\\_SEALNG2019reviewDIGITAL\\_compressed.pdf](https://sea-lng.org/wp-content/uploads/2020/02/200214_SEALNG2019reviewDIGITAL_compressed.pdf) (accessed on 18 December 2021).
16. Nautical Integrated Hybrid Energy System for Long-Haul Cruise Ships. 2020. Available online: <https://cordis.europa.eu/project/id/861647> (accessed on 18 December 2021).
17. Bloom Energy. Bloom Energy, Chantiers de l'Atlantique, and MSC Chart a Course for Cruise Ships Powered by Clean Energy. 2021. Available online: <https://www.bloomenergy.com/news/bloom-energy-chantiers-de-latlantique-and-msc-chart-a-course-for-cruise-ships-powered-by-clean-energy> (accessed on 18 December 2021).
18. Blue World and Alfa Laval develop marine methanol fuel cell unit. *Fuel Cells Bull.* **2021**, *2021*, 6. [CrossRef]
19. Nehter, P.; Wildrath, B.; Bauschulte, A.; Leites, K. Diesel Based SOFC Demonstrator for Maritime Applications. *ECS Trans.* **2017**, *78*, 171–180. [CrossRef]
20. Valadez Huerta, G.; Álvarez Jordán, J.; Dragon, M.; Leites, K.; Kabelac, S. Exergy analysis of the diesel pre-reforming solid oxide fuel cell system with anode off-gas recycling in the SchIBZ project. Part I: Modeling and validation. *Int. J. Hydrogen Energy* **2018**, *43*, 16684–16693. [CrossRef]
21. Valadez Huerta, G.; Álvarez Jordán, J.; Marquardt, T.; Dragon, M.; Leites, K.; Kabelac, S. Exergy analysis of the diesel pre-reforming SOFC-system with anode off-gas recycling in the SchIBZ project. Part II: System exergetic evaluation. *Int. J. Hydrogen Energy* **2018**, *44*, 10916–10924. [CrossRef]
22. Kistner, L.; Bensmann, A.; Hanke-Rauschenbach, R. Optimal Design of Power Gradient Limited Solid Oxide Fuel Cell Systems with Hybrid Storage Support for Ship Applications. *Energy Convers. Manag.* **2021**, *243*, 114396. [CrossRef]
23. Kistner, L.; Schubert, F.L.; Minke, C.; Bensmann, A.; Hanke-Rauschenbach, R. Techno-economic and Environmental Comparison of Internal Combustion Engines and Solid Oxide Fuel Cells for Ship Applications. *J. Power Sources* **2021**, *508*, 230328. [CrossRef]
24. Choi, E.J.; Yu, S.; Kim, J.M.; Lee, S.M. Model-Based System Performance Analysis of a Solid Oxide Fuel Cell System with Anode Off-Gas Recirculation. *Energies* **2021**, *14*, 3607. [CrossRef]
25. Lee, K.; Kang, S.; Ahn, K.Y. Development of a highly efficient solid oxide fuel cell system. *Appl. Energy* **2017**, *205*, 822–833. [CrossRef]
26. Wu, C.C.; Chen, T.L. Design and dynamics simulations of small scale solid oxide fuel cell tri-generation system. *Energy Convers. Manag. X* **2019**, *1*, 100001. [CrossRef]
27. Arteaga-Perez, L.E.; Casas, Y.; Peralta, L.M.; Kafarov, V.; Dewulf, J.; Giunta, P. An auto-sustainable solid oxide fuel cell system fueled by bio-ethanol. Process simulation and heat exchanger network synthesis. *Chem. Eng. J.* **2009**, *150*, 242–251. [CrossRef]
28. Kupecki, J.; Badyda, K. Mathematical model of a plate fin heat exchanger operating under solid oxide fuel cell working conditions. *Arch. Thermodyn.* **2013**, *34*, 3–21. [CrossRef]
29. Kupecki, J. Off-design analysis of a micro-CHP unit with solid oxide fuel cells fed by DME. *Int. J. Hydrogen Energy* **2015**, *40*, 12009–12022. [CrossRef]
30. Powell, M.; Meinhardt, K.; Sprenkle, V.; Chick, L.; McVay, G. Demonstration of a highly efficient solid oxide fuel cell power system using adiabatic steam reforming and anode gas recirculation. *J. Power Sources* **2012**, *205*, 377–384. [CrossRef]
31. Mai, A.; Iwanschitz, B.; Weissen, U.; Denzler, R.; Haberstock, D.; Nerlich, V.; Schuler, A. Status of Hexis' SOFC Stack Development and the Galileo 1000 N Micro-CHP System. *ECS Trans.* **2011**, *35*, 87–95. [CrossRef]
32. Peters, R.; Deja, R.; Blum, L.; Pennanen, J.; Kiviaho, J.; Hakala, T. Analysis of solid oxide fuel cell system concepts with anode recycling. *Int. J. Hydrogen Energy* **2013**, *38*, 6809–6820. [CrossRef]
33. Engelbracht, M.F.A.; Peters, R.; Blum, L.; Stolten, D. Analysis of a Solid Oxide Fuel Cell System with Low Temperature Anode Off-Gas Recirculation. *J. Electrochem. Soc.* **2015**, *162*, F982. [CrossRef]
34. van Biert, L.; Visser, K.; Aravind, P.V. A comparison of steam reforming concepts in solid oxide fuel cell systems. *Appl. Energy* **2020**, *264*, 114748. [CrossRef]
35. Martin, H.; Gnielinski, V. Calculation of Heat Transfer from Pressure Drop in Tube Bundles. In Proceedings of the 3rd European Thermal Sciences Conference, Heidelberg, Germany, 10–13 September 2000; Hahne, E.W.P., Heidemann, W., Spindler, K., Eds.; Edizioni ETS: Pisa, Italy, 2000; pp. 1155–1160.
36. VDI-Gesellschaft Verfahrenstechnik und Chemieingenieurwesen (Ed.) *VDI-Wärmeatlas*, 10th ed.; Springer: Berlin/Heidelberg, Germany, 2013. [CrossRef]
37. Roetzel, W.; Luo, X.; Chen, D. *Design and Operation of Heat Exchangers and Their Networks*; Academic Press an Imprint of Elsevier: London, UK; San Diego, CA, USA; Cambridge, MA, USA; Oxford, UK, 2020.
38. Luo, X.; Zhou, G.Y.; Cong, L.W.; Fuchs, M.; Kabelac, S. Numerical Simulation of Heat Transfer and Fluid Flow in 3D-Printed High-Temperature Plate-Fin Heat Exchangers with OpenFoam. In Proceedings of the 25th National and 3rd International ISHMT-ASTFE Heat and Mass Transfer Conference (IHMT-2019), Roorkee, India, 28–31 December 2019; Begellhouse: Danbury, CT, USA, 2019; pp. 569–574. [CrossRef]
39. Fuchs, M.; Heinrich, D.; Luo, X.; Kabelac, S. Thermal performance measurement of additive manufactured high-temperature compact heat exchangers. *J. Phys. Conf. Ser.* **2021**, *2116*, 012095. [CrossRef]
40. Kuppan, T. *Heat Exchanger Design Handbook*, 2nd ed.; Mechanical Engineering Series; CRC Press: Hoboken, NJ, USA, 2013; Volume 222.

41. ISO 16903:2015: *Petroleum and Natural Gas Industries—Characteristics of LNG, Influencing the Design, and Material Selection*; International Organization for Standardization: Geneva, Switzerland, 2015. Available online: <https://www.iso.org/standard/57891.html> (accessed on 18 December 2021).
42. Gubner, A. Non-Isothermal and Dynamic SOFC Voltage-Current Behavior. *ECS Proc. Vol.* **2005**, 2005-07, 814–826. [[CrossRef](#)]
43. Walter, C.; Schwarze, K.; Boltze, M.; Herbrig, K.; Surrey, A. Status of Stack & System Development at Sunfire. In Proceedings of the 14th European SOFC & SOE Forum (EFCF), Lucerne, Switzerland, 20–23 October 2020; pp. 29–38.
44. van Biert, L.; Godjevac, M.; Visser, K.; Aravind, P.V. Dynamic modelling of a direct internal reforming solid oxide fuel cell stack based on single cell experiments. *Appl. Energy* **2019**, *250*, 976–990. [[CrossRef](#)]
45. Çengel, Y.A.; Ghajar, A.J. *Heat and Mass Transfer: Fundamentals and Applications*, 6th ed.; McGraw-Hill Education: New York, NY, USA, 2020.
46. Wongchanapai, S.; Iwai, H.; Saito, M.; Yoshida, H. Performance evaluation of a direct-biogas solid oxide fuel cell-micro gas turbine (SOFC-MGT) hybrid combined heat and power (CHP) system. *J. Power Sources* **2013**, *223*, 9–17. [[CrossRef](#)]
47. Saarinen, J.; Halinen, M.; Ylijoki, J.; Noponen, M.; Simell, P.; Kiviaho, J. Dynamic Model of 5kW SOFC CHP Test Station. *J. Fuel Cell Sci. Technol.* **2007**, *4*, 397–405. [[CrossRef](#)]
48. Sarantaridis, D.; Atkinson, A. Redox Cycling of Ni-Based Solid Oxide Fuel Cell Anodes: A Review. *Fuel Cells* **2007**, *7*, 246–258. [[CrossRef](#)]
49. Angeli, S.D.; Monteleone, G.; Giaconia, A.; Lemonidou, A.A. State-of-the-art catalysts for CH<sub>4</sub> steam reforming at low temperature. *Int. J. Hydrogen Energy* **2014**, *39*, 1979–1997. [[CrossRef](#)]